

Fine- and Microstructure Observations of Trapped Diurnal Oscillations Atop Fieberling Seamount

Eric Kunze

School of Oceanography, University of Washington, Seattle, Washington

John M. Toole

Woods Hole Oceanographic Institution, Woods Hole, Massachusetts

Abstract. Fine- and microstructure profiles collected over Fieberling Seamount at $32^{\circ}26'N$ in the eastern North Pacific reveal (i) an anticyclonic vortex cap of relative vorticity $-0.50f \pm 0.15f$, (ii) intensified diurnal oscillations of 15 cm s^{-1} , and (iii) elevated turbulence levels of eddy diffusivity $K_p \approx 10 \times 10^{-4} \text{ m}^2 \text{ s}^{-1}$ co-existing in a 200-m thick layer atop the summit plain. The vortex is *not* a Taylor cap because a strong negative potential vorticity anomaly is associated with it. It is at least partially maintained against Ekman downwelling by rectification of the diurnal oscillation as evidenced by its fortnightly cycle. The diurnal oscillation is slightly subinertial and driven by the barotropic K_1 and O_1 diurnal tides. It closely resembles a seamount-trapped topographic wave, but (i) its energy maximum is 50 m above the bottom, (ii) its horizontal velocity vector turns counterclockwise with depth, and (iii) there is a 180° phase difference between its radial velocity u_r and the vertical displacement $\xi' = -T'/\bar{T}_z$, producing a net positive radial heat-flux $\langle u_r T' \rangle$. These features are more consistent with an upward-propagating vortex-trapped near-inertial internal wave with a slightly subinertial frequency allowed by the strong negative vorticity of the vortex cap. This wave would be encountering a vertical critical layer at the top of the cap where its energy would be lost to turbulence. Observed turbulence levels imply decay times for the wave of ~ 3 days, emphasizing the strongly forced nature of this system.

1. Introduction

The peaks of seamounts have been found to be sites of enhanced near-bottom semidiurnal, diurnal, and inertial currents with moored current-meters (Noble *et al.*, 1988; Noble and Mullineaux, 1989; Genin *et al.*, 1989; Padman *et al.*, 1992; Eriksen, 1991) and profilers (Kunze and Sanford, 1986; Kunze *et al.*, 1992). These elevated velocities support abundant populations of benthic filterfeeders (Genin *et al.*, 1986, 1992). However, little is known about how topography intensifies these currents. Kunze and Sanford (1986) interpreted their signal as a critically-reflected upward-propagating near-inertial wave based on the counterclockwise turning of the signal's horizontal velocity with depth. On the other hand, Genin *et al.* (1989), Eriksen (1991), Noble *et al.* (1994), and Brink (1995) report slightly subinertial diurnal tidal frequencies associated with the dominant motions above Fieberling Guyot, so they advance that the fluctuations are seamount-trapped topographic waves.

Sloping bottom topography will cause internal waves with characteristic slopes $Cg_z/Cg_H = k_H/k_z$ identical to the bottom slope α to be critically reflected to high wavenumbers (Wunsch, 1969; Phillips, 1977; Eriksen, 1982; 1985) and scattered (Baines, 1971; Bell, 1975; Gilbert and Garrett, 1989; Müller and Xu, 1992), dramatically amplifying internal-wave shear and strain, and turbulence production.

Sloping topography also allows bottom-trapped topographic waves with frequencies $\omega \leq N \sin \alpha$ (Rhines, 1970)

although nonplanar bathymetry will not trap superinertial frequencies $\omega > f$ (Huthnance, 1978). Brink (1989, 1990) and Chapman (1989) formulated a model for stratified seamount-trapped topographic waves. They showed that the gravest mode for Fieberling Guyot's geometry and stratification is slightly subinertial and nearly resonant with the diurnal tide.

A vortex cap is also expected over a seamount. Both potential vorticity-conserving Taylor cap dynamics (Hogg, 1973; Swaters and Mysak, 1985; Roden, 1987) and wave rectification over topography (Loder, 1980; Maas and Zimmerman, 1989a, 1989b; Haidvogel *et al.*, 1993) imply formation of an anticyclonic vortex over the seamount's summit. A Taylor cap would require an impinging geostrophic flow and, in the absence of damping, would have the same potential vorticity as the surrounding ocean. Stratification will limit the vertical extent of the vortex above the seamount (Zyryanov, 1981; Chapman and Haidvogel, 1992) to $H = fL/N \sim 100 \text{ m}$ for $f = 7.8 \times 10^{-5} \text{ s}^{-1}$, the buoyancy frequency $N = 4.3 \times 10^{-3} \text{ s}^{-1}$, and the radius of the seamount summit $L = 7 \text{ km}$.

To better understand the impact of seamounts on internal waves, tides, and turbulent mixing, fine- and microstructure profiles were collected over Fieberling Guyot during March 1991 (Montgomery and Toole, 1993). Here we use the profile time-series and surveys to characterize the temporal and spatial structure of the co-existing vortex cap, diurnal oscillations, and turbulence atop Fieberling Guyot's summit plain.

The vortex cap is ~ 200 -m thick and has core vorticities $\zeta = -0.50f \pm 0.15f$. The presence of the anticyclonic vortex cap raises the possibility that the observed diurnal oscillation is not a seamount-trapped topographic wave but a vortex-trapped near-inertial internal wave (Kunze, 1986; Kunze *et al.*, 1995; Appendix A).

The coinciding diurnal shear layer is also 200-m thick. Maximum velocities of 15 cm s^{-1} are found 50–100 m above the bottom over the summit plain, unlike the bottom-intensified seamount-trapped wave (Brink, 1995). This signal decays rapidly as one moves radially off the summit. At any instant and depth, the horizontal velocity of the diurnal wave forms a unidirectional jet over the summit plain. This horizontal structure is consistent with either a gravest seamount-trapped mode (Brink, 1990) or a gravest vortex-trapped internal wave mode (Kunze *et al.*, 1995). The velocity vector turns counterclockwise with depth over the entire 200-m thick layer of intensified motion. This turning corresponds to a vertical wavelength $\lambda_z = 250 \text{ m}$. If interpreted as a vortex-trapped near-inertial wave, it implies upward energy propagation. It contradicts Brink's predicted turning of only $\sim 90^\circ$ confined to within 50 m of the bottom due to a time-dependent bottom Ekman layer.

Elevated turbulence levels of $\varepsilon \approx 10^{-7} \text{ W kg}^{-1}$ are found coincident with the vortex cap and the diurnal oscillation, corresponding to eddy diffusivities of $10 \times 10^{-4} \text{ m}^2 \text{ s}^{-1}$. This is sufficient to drain the wave in ~ 3 days if it is the energy source for the turbulence. The eddy diffusivity over the summit plain is not sufficiently enhanced for seamounts to play a dominant role in global mixing of the pycnocline.

2. Trapped Wave Models

Two extant models may describe the diurnal shear layer observed above the summit plain of Fieberling Guyot—seamount-trapped topographic waves (Brink, 1989, 1990) and vortex-trapped near-inertial internal waves (Kunze *et al.*, 1995; Appendix A). These two types of waves share many properties in common and their observable differences are subtle.

2.1 Seamount-Trapped Topographic Waves

Brink (1989, 1990) and Chapman (1989) formulated a model for seamount-trapped waves on tall seamounts in a stratified, rotating fluid, extending the barotropic models of Rhines (1969), Huthnance (1974), Hunkins (1986), and Kowalik (1994). These waves are bottom-trapped topographic waves (Rhines, 1970) wrapped around a seamount so that their along-isobath wavenumber is quantized. Laboratory experiments (Codiga, 1993; Boyer and Zhang, 1990; Zhang and Boyer, 1993) and numerical simulations (Haidvogel *et al.*, 1993) have verified generation of

seamount-trapped oscillations by barotropic subinertial forcing in stratified, rotating fluids.

For the stratification profile and geometry of Fieberling Guyot, Brink showed that the gravest-mode (highest frequency) seamount-trapped wave had a slightly subinertial frequency that was nearly resonant with the diurnal tide. This mode evanesces rapidly away from the bottom with a vertical decay scale of $\sim 50 \text{ m}$ and a radial decay scale of a few kilometers (radial mode 0). It propagates clockwise around the seamount with azimuthal mode $n = -1$. The first azimuthal mode is most likely to be excited by largescale forcing because it has flow in the same direction on opposite sides of the seamount (Brink, 1990). The resulting jet rotates clockwise in time. Observationally, Brink's predictions are consistent with the diurnal frequency and horizontal structure of the dominant velocity fluctuations above the summit plain of Fieberling Seamount (Eriksen, 1991; Noble *et al.*, 1994; Brink, 1995).

Of particular importance for distinguishing gravest seamount-trapped waves from vortex-trapped waves is that their radial velocity u_r' and vertical displacement ξ' signals are 90° out of phase (section 2.2). This implies that inviscid seamount-trapped waves have zero radial heat-flux $\langle u_r' T' \rangle$. Also, the horizontal velocity vector undergoes 180° reversals, but no turning, with depth. The addition of bottom friction might produce a counterclockwise-turning-with-depth, time-dependent benthic Ekman layer of thickness and turning scale

$$k_z^{-1} \sim \sqrt{\frac{V_e}{|\omega_i - f_{\text{eff}}|}} \quad (1)$$

(Maas and van Haren, 1987), where the intrinsic frequency $\omega_i = \omega_E - nV_\theta/r \approx \omega_E - n\zeta/2 = K_1 + \zeta/2\omega_E$ is the Eulerian frequency, V_θ is the horizontal velocity of the vortex, and $f_{\text{eff}} = f + \zeta$. However, (1) depends on the profiles of turbulence and stratification. Eddy viscosity will also alter the phase relations but only by a few degrees (Appendix C).

2.2 Vortex-Trapped Near-Inertial Internal Waves

The anticyclonic vortex above the summit plain with core vorticity $-0.50f$ is sufficient to reduce the lower bound of the internal waveband from the planetary Coriolis frequency f to an effective Coriolis frequency $f_{\text{eff}} = f + \zeta$ (Weller, 1982; Kunze, 1985; Kunze, 1986), well below the diurnal frequencies $K_1 = 0.933f = 1.87f_{\text{eff}}$ and $O_1 = 0.865f = 1.73f_{\text{eff}}$. This allows diurnal frequencies to propagate as near-inertial internal waves within the confines to the negative vorticity core. Kunze *et al.* (1995) formulated a model for a vortex-trapped near-inertial radial mode while investigating near-inertial wave critical layers in a warm-core ring. The superposition of plane waves reflecting off the lateral sides of the vortex sets up a radial mode that closely resembles a seamount-

trapped wave in its horizontal structure. Like the seamount-trapped wave, the most likely azimuthal mode for largescale forcing is $n = -1$, corresponding to clockwise azimuthal propagation around the vortex. The intrinsic, or Lagrangian, frequency then is $\omega_i = \omega_E - nV_\theta/r \approx K_1 + \zeta/2 = 0.933f - 0.25f = 0.683f > f_{eff} = f + \zeta = 0.50f$. Like the gravest seamount-trapped wave, this mode has maximum velocity amplitudes near vortex center and, at any given instant, forms a nearly unidirectional jet in the vortex core that rotates clockwise in time. Decay is rapid moving radially out of the vortex.

Unlike the seamount-trapped topographic wave, a vortex-trapped wave is an internal wave and is therefore free to carry energy and momentum upward into the overlying water column. For a near-inertial wave of upward energy propagation, the horizontal velocity vector turns counterclockwise with depth. The associated vertical wavelength is

$$\lambda_z = \lambda_r \sqrt{\frac{\omega_i^2 - f_{eff}^2}{N}}, \quad (2)$$

where λ_r is the radial wavelength (Appendix A, Kunze *et al.*, 1995). Since the wave can propagate freely only inside the vortex, its energy will accumulate in a vertical critical layer at the top of the core until instabilities transfer it to turbulence production and mixing (Kunze *et al.*, 1995). Thus, for a vortex-trapped wave, energy, shear, and turbulent dissipation maxima above the bottom are expected. For upward and clockwise azimuthal propagation, the radial velocity u'_r is 180° out of phase with the vertical displacement $\xi' = -T'/\bar{T}_z$, for a net outward radial heat-flux $\langle u'_r T' \rangle$.

Including an eddy viscosity of $10 \times 10^{-4} \text{ m}^2 \text{ s}^{-1}$, consistent with the microstructure measurements, does not significantly alter the dispersion relation between frequency, vertical wavenumber, and horizontal wavenumber (2), or the consistency relations between horizontal velocity components u'_r and v'_θ , and thus will not alter the turning with depth. The phase relation between a viscous wave's vertical displacement ξ' and the horizontal velocities is modified by at most 6° for the vertical wavelengths of interest (Appendix B).

2.3 Summary of Commonalities and Differences

In the context of Fieberling Seamount, seamount- and vortex-trapped waves share the following properties:

- Both are forced by the barotropic diurnal tide, so their Eulerian frequencies $\omega_E = \omega_i + nV_\theta/r \approx \omega_i - \zeta/2 = K_1, O_1$.
- The horizontal velocity vectors of both rotate in time with the radial and azimuthal velocities 90° out of phase above the summit plain.
- Both propagate clockwise azimuthally around the seamount (azimuthal mode $n = -1$).

- Both decay radially away from the seamount.

The differences are more subtle:

- The vortex-trapped wave requires a vortex of sufficient strength to permit a diurnal Eulerian frequency. The seamount-trapped wave does not and will not exist if the frequency is effectively superinertial.
- The vortex-trapped wave will carry energy and momentum into the stratified water column and thus can have an energy maximum above the bottom (upward energy propagation implies counterclockwise turning of the horizontal velocity vector with depth). The seamount-trapped wave is a bottom-trapped topographic wave so it should have its maximum signal at the bottom and little turning of the velocity vector with depth. (Bottom friction might induce a time-dependent benthic Ekman layer having counterclockwise turning with depth.)
- The radial velocity u'_r and temperature T' fluctuations for vortex-trapped waves propagating upward and clockwise around the vortex are in phase so produce a net outward radial heat-flux $\langle u'_r T' \rangle$. (In the absence of dissipative processes, the divergences of this heat-flux and a nonzero vertical momentum-flux $\langle v'_\theta w' \rangle$ drive a wave-induced mean circulation \bar{u}_r and \bar{w} which exactly counterbalance the wave fluxes and there is no net change to the background mean fields; see Appendix A.) For inviscid seamount-trapped waves, the radial heat-flux is zero. These phase relations are only slightly modified by inclusion of eddy viscous effects (Appendices B and C).

3. Measurements and Analysis

3.1 Data

Profiles were collected over the summit and flanks of Fieberling Guyot ($32^\circ 26' \text{N}$, $127^\circ 45' \text{W}$) with the High-Resolution Profiler (HRP; Schmitt *et al.*, 1988), Sippican expendable current profilers (XCPs; Sanford *et al.*, 1982; Sanford *et al.*, 1993), and Sippican T-5 (1600-m) expendable bathythermographs (XBTs) in March 1991 as part of the ONR-sponsored Abrupt Topography Program to investigate the impact of seamounts on physical and biological oceanography. At the seamount's latitude, the Coriolis frequency is $7.8 \times 10^{-5} \text{ s}^{-1}$ (22.4 h), so both the K_1 (24.0 h, $0.933f$) and O_1 (25.9 h, $0.865f$) diurnal tides are subinertial. Barotropic diurnal tides propagate north west here (Schwiderski, 1981a, b).

Fieberling Guyot rises from an abyssal plain of 4000–4500-m depth to a summit plain at 500–700-m depth (Fig. 1). A narrow pinnacle southwest of the geometric center of the summit plain attains 440-m depth. By definition, a guyot has a flat top (apart from the pinnacle). Radial bottom slopes on the summit plain are ~ 0.05 compared to flank slopes exceeding 0.2. The abrupt change in

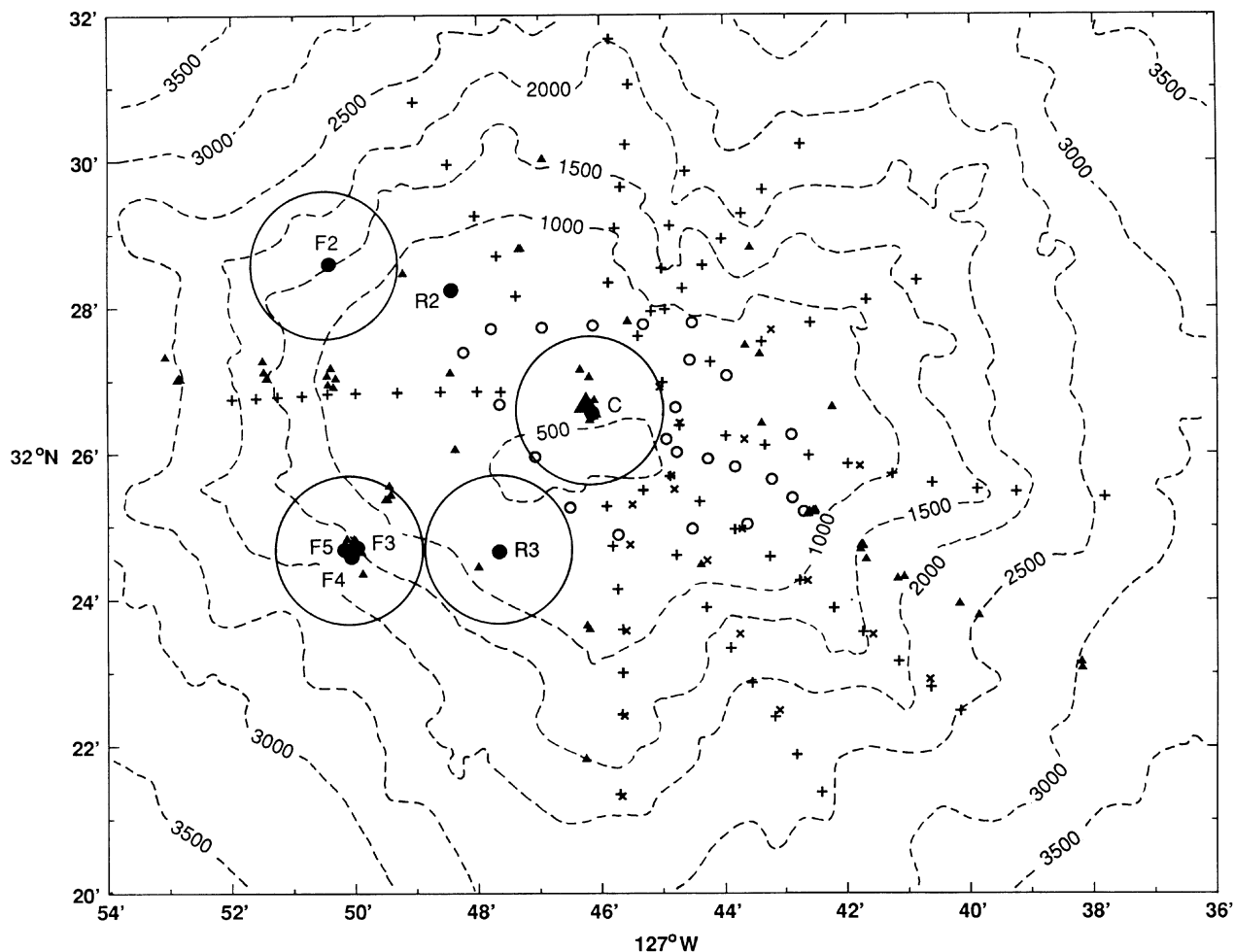


Figure 1. Velocity profiler stations (XCP, +, x, o; HRP, \blacktriangle) and current-meter mooring sites (\odot) over the summit plain and flanks of Fieberling Guyot. Bathymetry is in meters. HRP measurements consist of day-long profile time-series at C and F3, spoke time-series to the west and southeast, and a survey around the rim. Radial XCP spokes were made from seamount center to the 2500-m isobath. Surveys to the south and east were collected on 7 March 1991 (+, x), to the north and west on 8 March (+), and on the summit plain on 18 March (o).

slope near the 700-m isobath will be referred to as the summit rim and has an average radius of 5 km. The summit plain is elongated so that the rim radius is about 6.5 km zonally and half that meridionally (Fig. 1). Beyond the rim, Fieberling Guyot can be described as a Gaussian of radial scale $r = 12$ km (Codiga, 1991). It is the northwesternmost of the Fieberling seamount chain. For the motions on the summit plain discussed here, Fieberling appears to be dynamically isolated from its nearest neighbor, Fieberling II, which lies 40 km to the southeast. This is consistent with the conclusion of Roden (1991) that only in the abyss did the seamount chain affect background impinging currents as a group.

Other relevant measurements are two mesoscale CTD surveys conducted in August 1989 (Roden, 1991) and in April–May 1991 (Roden, 1994) and year-long current-meter mooring deployments from September 1990 to

September 1991 at seven sites on Fieberling Guyot and the abyssal plain to the west (Wichman *et al.*, 1993; Noble *et al.*, 1994; Brink, 1995; Eriksen, 1995). The moorings were sited at the center of the summit plain (C in Fig. 1), to the northwest and southwest on the rim (R2 and R3), to the northwest and southwest in 1500-m water on the flanks (F2 and F3–5), and 40 km to the northwest and southwest on the abyssal plain.

The HRP measurements include day-long time-series sampled every 3 h at the central (C) and southwest flank (F3) mooring sites, repeated radial sections to the 3000-m isobath over the western and southeastern flanks, and a survey around the rim (Fig. 1). Profiles 20–40 km from the peak on the neighboring abyssal plain are described by Toole *et al.* (1994). The stratified turbulent benthic boundary layer overlying the flanks is discussed by Toole *et al.* (1995).

The HRP is a freefall profiler (Schmitt *et al.*, 1988). Its sensor suite includes a CTD and a two-axis acoustic current-meter which provide finescale vertical profiles of temperature, salinity, pressure, and horizontal velocity relative to an unknown but depth-independent constant. Also included are a high-speed thermistor, a dual-needle conductivity probe, and airfoil velocity shear probes to estimate microscale temperature and velocity dissipation rates. Schmitt *et al.* (1988) and Polzin (1992) detail the reduction of the microstructure data which follows the methodology developed by Neil Oakey at the Bedford Institute of Oceanography—half-meter segments of microstructure data are windowed, Fourier-transformed, and corrected for sensor and electronic interface responses. Gradient variances are then estimated by integrating the gradient spectra out to a spectral minimum (beyond which instrument noise dominates). Dissipation rate estimates assume three-dimensional isotropy. The production/dissipation balances of Osborn and Cox (1972) and Osborn (1980) are used to obtain diapycnal eddy diffusivity estimates, employing a mixing efficiency of 0.25 (Oakey, 1982).

For the seamount cruise, HRP was equipped with a Sea-Data Inc. acoustic altimeter to trigger release of the descent weight when the profiler got within 10 m of the bottom. The weight-release criterion was effective over the summit plain but less reliable over the steep flanks (presumably because of poor acoustic backscatter). HRP dives frequently terminated up to 100 m above the bottom, and one made contact with the bottom.

Most of the XCPs were deployed along radial spokes from near the center of the summit plain to the 2500-m isobath on the flanks of the guyot (Fig. 1). XCP profiles in water depths less than 1600 m measured into the bottom. A survey of 43 profiles was conducted to the south and east between 0800 and 1300 hours on 7 March (+), with 19 of the stations being reoccupied between 1330 and 1730 hours (X). A survey of 34 profiles was conducted to the north and west between 0500 and 0900 hours on 8 March (+). Finally, a survey of 24 profiles was conducted over the summit plain a week and a half later between 0500 and 0830 hours on 18 March (o). Most of the XCP data were collected within a few hours of the same phase of the diurnal tide. No expendable probes were dropped within 1 nmi of the moorings to prevent fouling of the current-meter rotors with expendable wire. As a result, the southwest quadrant was undersampled.

The expendable current profiler (XCP) measures the horizontal velocity to within an unknown but depth-independent constant using the voltage drop induced by seawater's motion through Earth's magnetic field and measures temperature with an XBT thermistor to 1600-m

depth. Preanalysis processing averages the data in 3-m bins, with typical rms errors of $\pm 0.4 \text{ cm s}^{-1}$ and $\pm 0.06^\circ\text{C}$ for velocity and temperature, respectively.

3.2 Analysis

Two features predicted to occur atop a seamount are (i) a vortex cap, which should be axisymmetric and dominantly in the azimuthal velocity v_θ , and (ii) an azimuthal-mode-one seamount- or vortex-trapped wave forced by the barotropic diurnal tide, which should consist of a unidirectional, slightly subinertial jet over the summit which turns clockwise in time (see Fig. 15).

The vortex and wave signals will be separated in the profile surveys by azimuthal averaging $\langle \cdot \rangle_\theta$. Averaging the east and north velocities filters out axisymmetric flow, isolating the expected diurnal wave signal. Averaging azimuthal and radial velocities filters out all azimuthal modes except mode zero, isolating the axisymmetric vortex. We caution that numerical simulations do not always find the vortex to be axisymmetric (Haidvogel *et al.*, 1993). While it might be preferable to fit the data to azimuthal modes as done by Codiga (1995), the present scheme captures the dominant signals above the summit plain and produces results indistinguishable from those of modal fitting. The coordinate system is centered on the seamount centroid ($32^\circ 26.2' \text{N}$, $127^\circ 45.5' \text{W}$) as determined by Codiga (1991). The unknown barotropic offset is handled by arbitrarily removing the depth-average between 150 and 300 m before azimuthal averaging. This emphasizes perturbations at the summit depth and below. To compensate for the nonuniform azimuthal sampling (Fig. 1), the azimuthal averages are weighted by the sampling in the N, W, S, and E quadrants. This works for the velocity signals but may not handle the dipolar temperature (displacement) signal around the seamount adequately. Toole *et al.* (1995) explore the effects of averaging relative to local bathymetry orientation.

4. The Vortex Cap

4.1 Spatial Structure

Radial sections of azimuthally-averaged radial velocity $\langle u_r \rangle_\theta$ and azimuthal velocity $\langle v_\theta \rangle_\theta$ are displayed in Fig. 2. The profiles have been WKB-stretched to

$$N_0 = 5.2 \times 10^{-3} \text{ s}^{-1} \left[z \rightarrow \int_z^0 (N(z)/N_0) dz \right]$$

to remove variations in the vertical scale and amplitude due solely to changes in the buoyancy frequency N . True depths are indicated along the right axes.

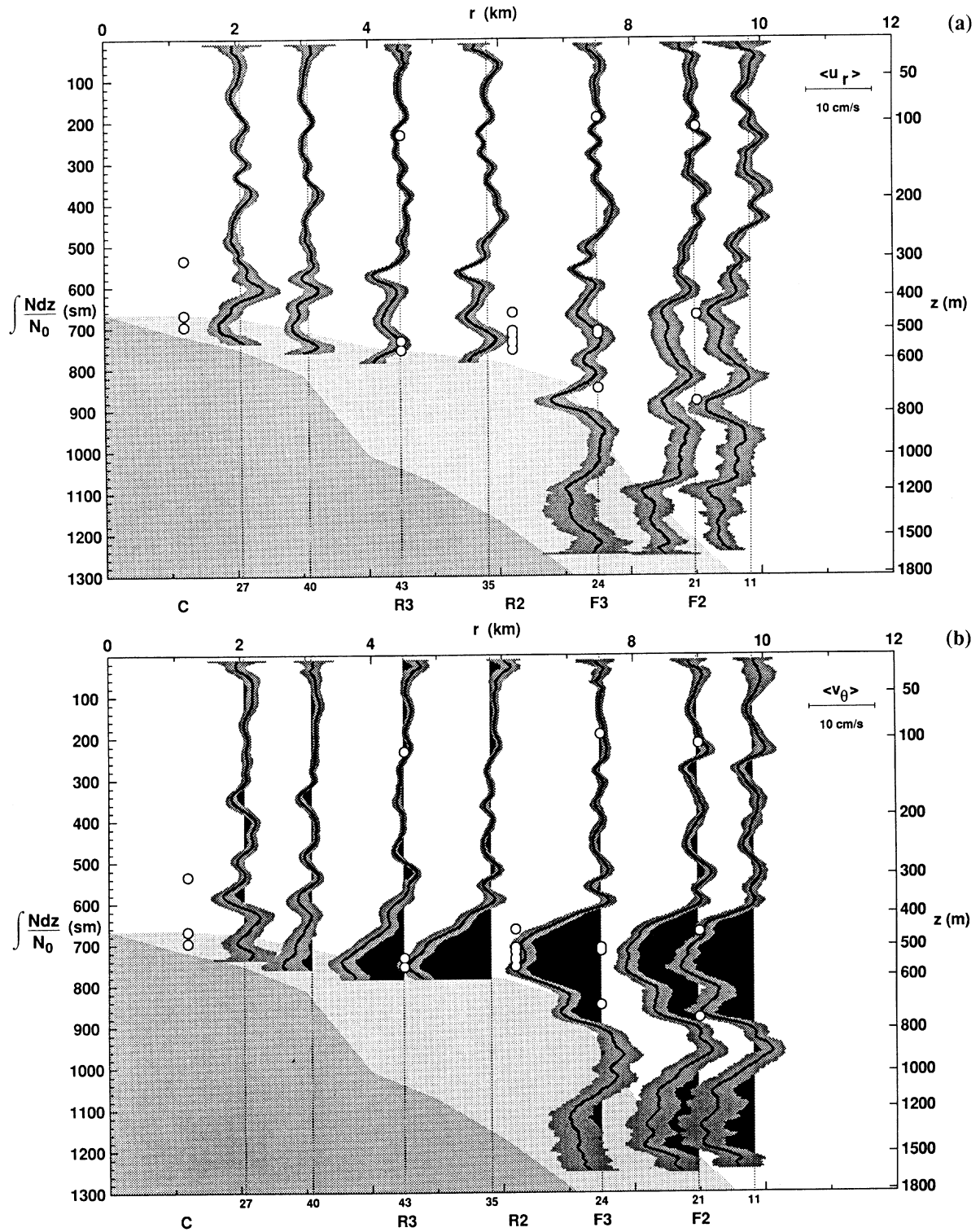


Figure 2. Radial profile sections of azimuthally-averaged (a) radial velocity $\langle u_r \rangle_\theta$ and (b) azimuthal velocity $\langle v_\theta \rangle_\theta$ with one standard error indicated by dark shading. Uneven azimuthal sampling (Fig. 1) is compensated for before averaging. The depth coordinate (left axis) has been WKB-stretched with respect to $N_0 = 5.2 \times 10^{-3} \text{ s}^{-1}$; true depths are shown along the right axis. Numbers along the bottom axis correspond to the number of drops going into each average, darker and lighter silhouettes to extremes in the WKB-normalized bathymetry, and open circles to current-meter sites. The radial velocity $\langle u_r \rangle_\theta$ (a) is everywhere less than 2 cm s^{-1} . The azimuthal velocity $\langle v_\theta \rangle_\theta$ (b) exhibits anticyclonic flow of up to 10 cm s^{-1} over the summit rim at 6–8 km radius between 600 and 900 m (400- and 800-m depth).

Radial velocities (Fig. 2a) are everywhere less than 2 cm s^{-1} . The uniformly weak radial flows suggest that our azimuthal averaging scheme is not biased. At some depths, e.g., 580 sm (stretched meters), there is a suggestion of persistent in- or outflow. These instances are of such small vertical scale that we hesitate to equate them with the $1\text{--}2 \text{ cm s}^{-1}$ radial outflow reported near the bottom by Eriksen (1991) and Brink (1995) because of possible problems with azimuthal nonuniformity, because of the short duration of our sampling, and because the profile surveys were collected during a time of relatively weak radial flow as inferred from the R2 ADCP velocities (see Fig. 6).

The average azimuthal velocity (Fig. 2b) displays a much more clearly defined signal. A 200-sm thick layer of anticyclonic flow resides atop the summit plain. Maximum speeds of $\sim -10 \text{ cm s}^{-1}$ are found at the rim (radius $r = 7 \text{ km}$). The vortex is bounded above by a 100-m thick $\partial \langle v_\theta \rangle_\theta / \partial z = 1.5 \times 10^{-3} \text{ s}^{-1} = 0.3 \bar{N}$ vertical shear layer and below by a 200-m thick $10^{-3} \text{ s}^{-1} = 0.25 \bar{N}$ shear layer. Corresponding relative vorticities $\zeta = \partial \langle v_\theta \rangle_\theta / \partial r + \langle v_\theta \rangle_\theta / r$ (Fig. 3) are noisier because they involve derivatives. The vorticity has values of $-0.50f \pm 0.15f$ over the summit plain and vanishes over the seamount flanks so, in the vortex core, the effective Coriolis frequency $f_{\text{eff}} = 0.5f = 2\pi/(44.8 \text{ h}) < K_1, O_1$.

Freeland (1994) observed a 40-m thick vortex cap of similar strength in ADCP surveys atop Cobb Seamount that was steady on 6–7 day timescales. However, during a different cruise, Codiga (1995) found vorticities weaker than $-0.1f$ atop Cobb. There is a hint that the vorticity vanishes inside a 2-km radius (Fig. 3), but vortex center position uncertainties are large enough that this cannot be stated conclusively. The absence of a positive vorticity annulus outside the azimuthal velocity maximum indicates that the azimuthal velocity $\langle v_\theta \rangle_\theta$ falls off as r^{-1} for radii $r > 7 \text{ km}$.

4.2 Comparison with Current-Meter Observations

Figures 4 and 5 compare the XCP vorticities and azimuthal velocities with 2-day averages of the current-meter records (Wichman *et al.*, 1993) about the time of the 7–8 March XCP surveys. The current-meter relative vorticity is inferred assuming solid-body rotation, $\zeta = 2V_\theta / r$. The current-meter data verify anticyclonic swirling between 400- and 600-m depth (Fig. 4), albeit slightly stronger. The current-meters and profilers also both reveal nearly solid-body rotation inside 7-km radius (Fig. 5). Azimuthal currents fall off more slowly in the current-meter data than in the profile data at larger radii. Mean flows shallower than 400 m are weak and show no reluctance to cross isobaths.

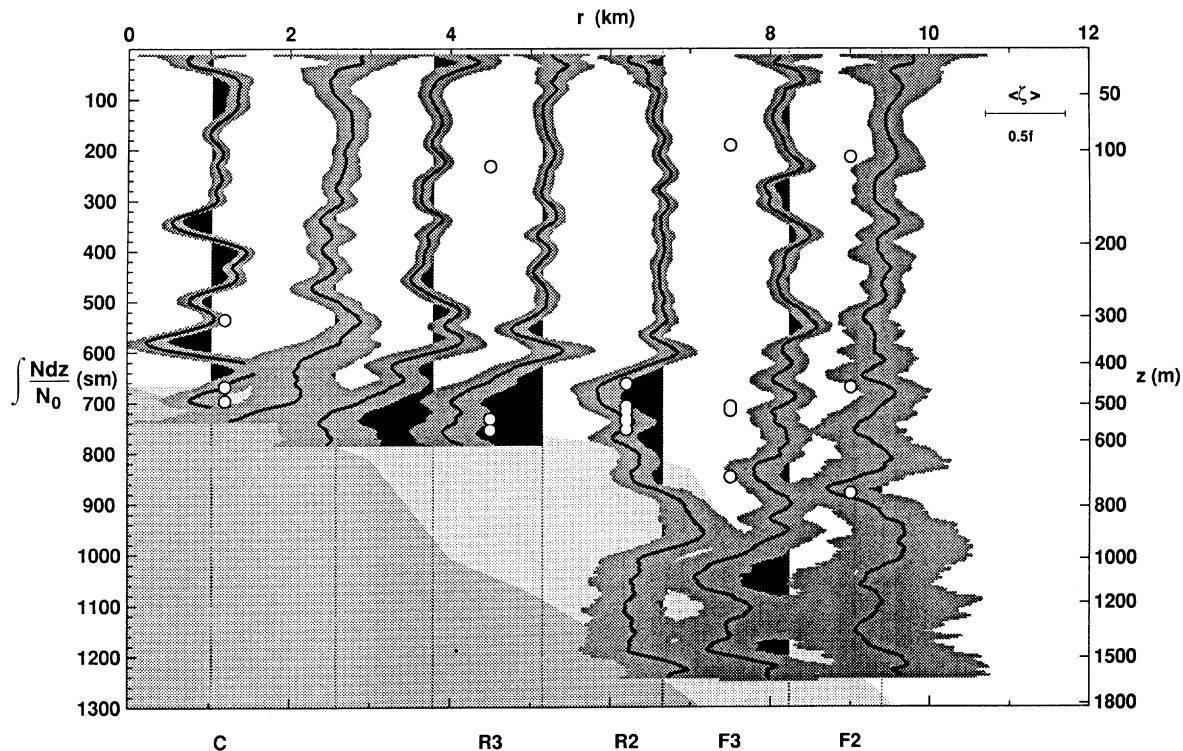


Figure 3. Radial profile sections of azimuthally-averaged relative vorticity $\langle \zeta \rangle_\theta = \partial \langle v_\theta \rangle_\theta / \partial r + \langle v_\theta \rangle_\theta / r$ with one standard error indicated by dark shading. Relative vorticities of $\sim -0.50f \pm 0.15f$ are found in a 200-m thick layer over the summit plain. Vorticities vanish at radii $r > 8 \text{ km}$, indicating that $\langle v_\theta \rangle_\theta \propto r^{-1}$. Weak vorticities inside 2-km radius may reflect measurement uncertainty in the position of the vortex center.

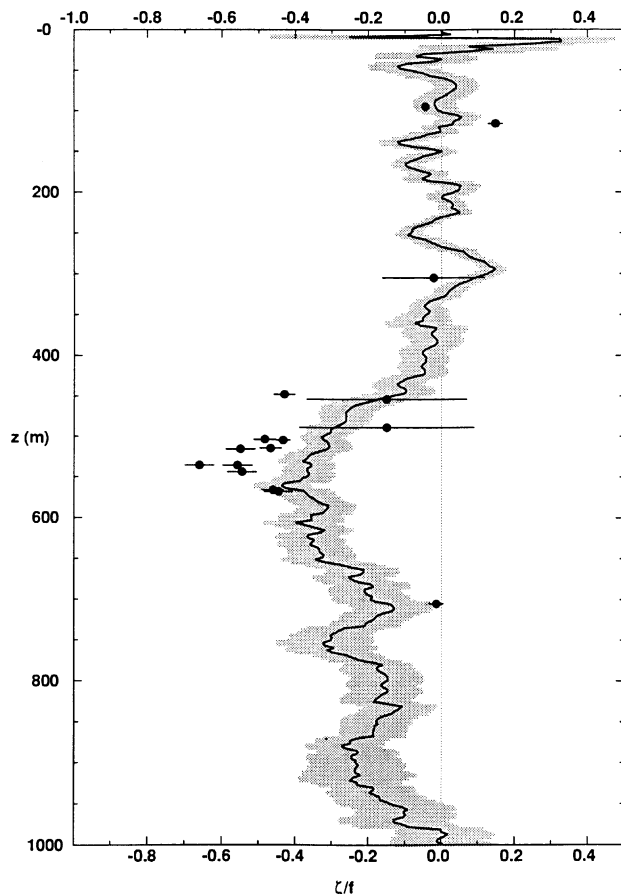


Figure 4. Comparison of the vertical structure of the relative vorticity at $r = 6.7$ km from the XCP surveys (solid curve) with 4-day smoothed current-meter vorticities $\zeta \approx 2\langle v_\theta \rangle_t / r$ (\leftrightarrow) from inside 7-km radius at the time of the XCP surveys assuming solid-body rotation. XCP vorticities are $-0.35f$ to $-0.40f$ between 500- and 650-m depth, vanishing abruptly shallower than 400 m and more gradually deeper than 900 m. Current-meter vorticities are slightly stronger at $-0.5f$ to $-0.6f$.

Differences between profiler and current-meter velocities likely arise because the two measurements do not sample the same part of the flow. If the vortex is not perfectly circular, is off center, or is otherwise not axisymmetric as found in numerical simulations (Haidvogel *et al.*, 1993), differences in the profiler and current-meter estimates would result.

4.3 Temporal Behavior

Fortnightly modulation of the vortex strength is apparent in 2-day smoothed azimuthal velocities from the rim moorings (e.g., at R2, Fig. 6). This implies that the vortex cap, with its dome of cold water over the seamount peak, is at least partially sustained against benthic Ekman pumping and turbulent decay by rectification of the K_1 and O_1 tidal fluctuations. In particular, Eriksen (1991) and Brink (1995) argue that diurnal-wave radial heat-fluxes balance downward Ekman pumping over the

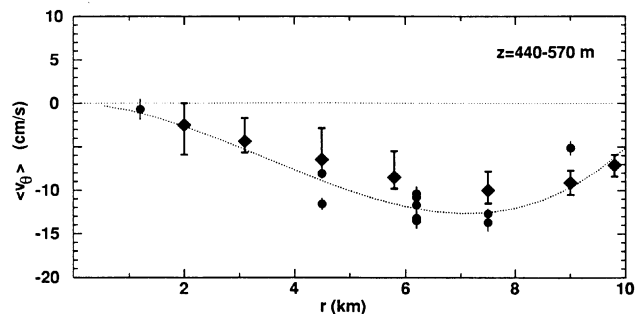


Figure 5. Comparison of the radial dependence of 4-day smoothed current-meter and azimuthally-averaged XCP azimuthal velocities, $\langle v_\theta \rangle_t$ ($+$) and $\langle v_\theta \rangle_\theta$ (\blacklozenge), in the depth range 440–570 m. The dotted line is a cubic least-squares fit setting $\langle v_\theta \rangle = 0$ at $r = 0$ and $r = 11$ km. The current-meters indicate extreme azimuthal velocities of -14 cm s^{-1} at $r = 6\text{--}7.5$ km with near solid-body rotation at smaller radii. XCPs indicate a similar structure but slightly weaker velocities of $\sim -10 \text{ cm s}^{-1}$.

summit plain. Freeland (1994) suggested that the vortex observed atop Cobb Seamount was forced by wave rectification also. This raises the question of whether the vortex cap on Fieberling's summit is a Taylor cap or maintained entirely by rectified tidal flux-divergences, and raises doubts about past oceanographic interpretations of isopycnal doming over seamounts in terms of Taylor cap dynamics. Wave rectification induced by intense dissipative processes appears to be at least as important a driving mechanism here but is poorly understood.

The R2 current-meter time-series show that the vortex abruptly turns on and off every few months (Fig. 6). The same behavior is seen at R3. Brink (1995) argues that this is a function of the impinging zonal flow direction. His Fig. 13 shows a tendency for a vortex cap to be present during eastward flow in the far field and suppressed during westward flow. This is contrary to β -plane dynamics predictions. McCartney (1975) and Verron and LeProvost (1985) find that westward flow produces trapped vortices while eastward flow generates a Rossby wave wake in barotropic β -plane simulations of flow past a small-amplitude seamount. The HRP and XCP measurements were taken at a time of transition from weak eastward to weak westward impinging flow ($\bar{u} \approx \pm 1 \text{ cm s}^{-1}$). Since the vortex flow exceeds the impinging flow, the fluid it contains is isolated.

4.4 Potential Vorticity Anomaly

Even though the HRP profiles reveal a 200-m thick positive density anomaly ($\langle \delta \sigma_\theta \rangle = 0.02 \text{ m}$, Fig. 7a) associated with the vortex cap atop the summit plain (site C, $r \sim 1$ km) compared to the flank (F3, $r = 7.5$ km), corresponding to an upward vertical displacement of 4 m, it is too weak to produce a discernible buoyancy frequency

FIEBERLING R2

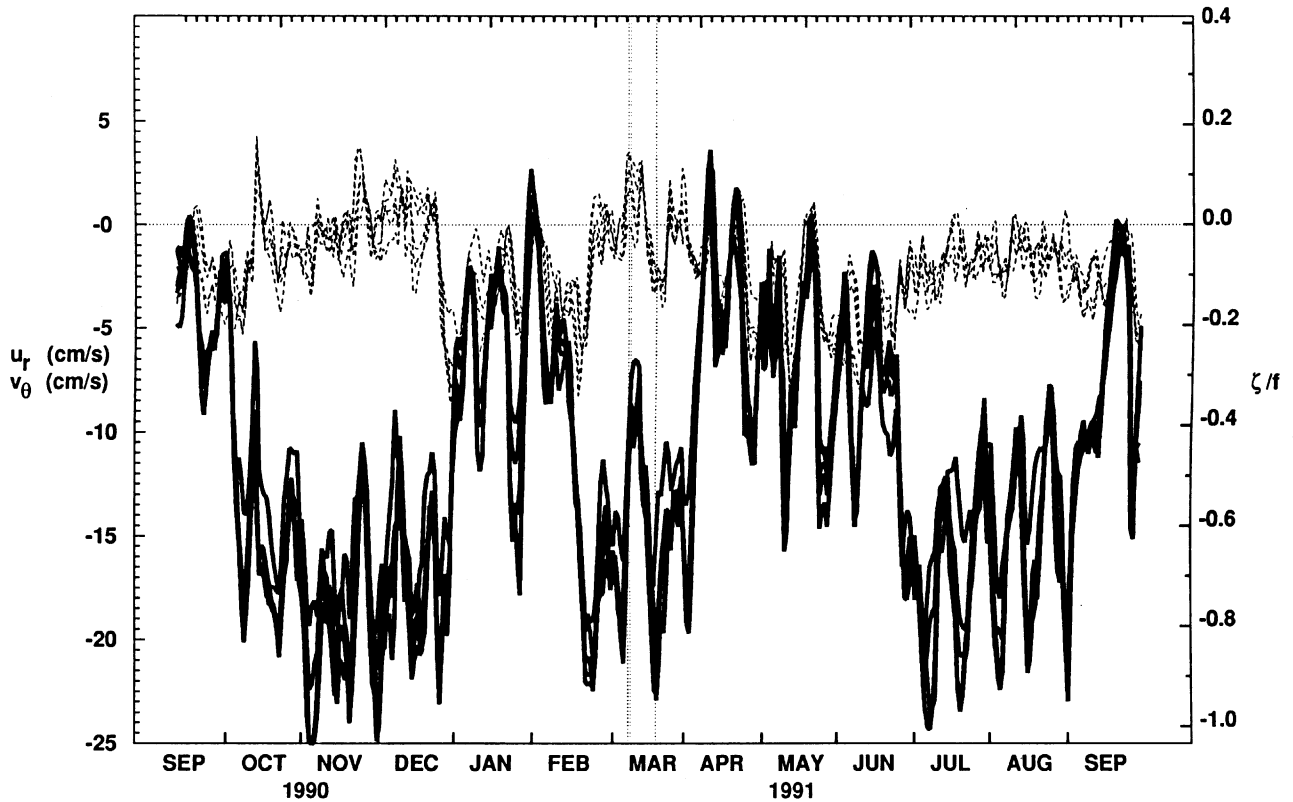


Figure 6. Time-series of 4-day smoothed azimuthal velocity $\langle v_\theta \rangle_t$ (solid) and radial velocity $\langle u_r \rangle_t$ (dotted) from the upward-looking ADCP at R2 on the summit plain's rim (Fig. 1) in the depth range 500–570 m (700–750 m). The azimuthal velocity is also expressed as a relative vorticity (right axis) assuming solid-body rotation, $\zeta = 2\langle v_\theta \rangle_t / r$. XCP survey periods are indicated by dotted vertical lines. The radial velocity tends to be less than $\pm 5 \text{ cm s}^{-1}$ while the azimuthal velocity is consistently negative. Fortnightly fluctuations in $\langle v_\theta \rangle_t$ are of insufficient strength to shut off or reverse its direction. Every 2–3 months, the azimuthal velocity abruptly shifts between $\sim 15\text{--}20 \text{ cm s}^{-1}$ and $\sim 5 \text{ cm s}^{-1}$ accompanied by less dramatic changes in the radial velocity.

anomaly. As a result, the relative vorticity of the vortex cap induces a negative potential vorticity anomaly of $-0.25 \bar{f} N^2$ (Fig. 7b) only slightly diminished by the weak positive buoyancy frequency anomaly. The presence of a potential vorticity anomaly is *not* consistent with pure Taylor cap dynamics, which preserves potential vorticity. Irreversible dissipative processes, such as those associated with wave rectification, must play a role in creating a potential vorticity anomaly (Ertel, 1942; Haynes and McIntyre, 1987). Viscous damping and bottom friction by themselves would produce a positive anomaly and thus cannot be responsible for the observed anomaly. If features like this potential vorticity anomaly are occasionally shed off seamounts, they might explain the submesoscale potential vorticity anomalies found beside Ampere Seamount by Kunze and Sanford (1993).

4.5 Cyclogeostrophic Balance

The subinertial azimuthally-averaged radial momentum equation can be expressed

$$\boxed{\frac{V_\theta^2}{r} + fV_\theta} = \frac{\partial P}{\partial r} + \frac{\partial \langle u_r'^2 \rangle}{\partial r} + \frac{\langle u_r'^2 \rangle - \langle v_\theta'^2 \rangle}{r} + \frac{\partial \langle u_r' w' \rangle}{\partial z}, \quad (3)$$

where the reduced, or kinematic, pressure $P = P/\rho_0$ and P is the dynamic pressure. The boxed terms are the cyclogeostrophic (gradient-wind) balance expected for steady inviscid flow with curvature in the absence of strong forcing, e.g., rings and Meddies. We will refer to the lefthand side of (3) as the effective Coriolis acceleration. Figure 8 compares the right- and lefthand sides of a radially-integrated cyclogeostrophic balance

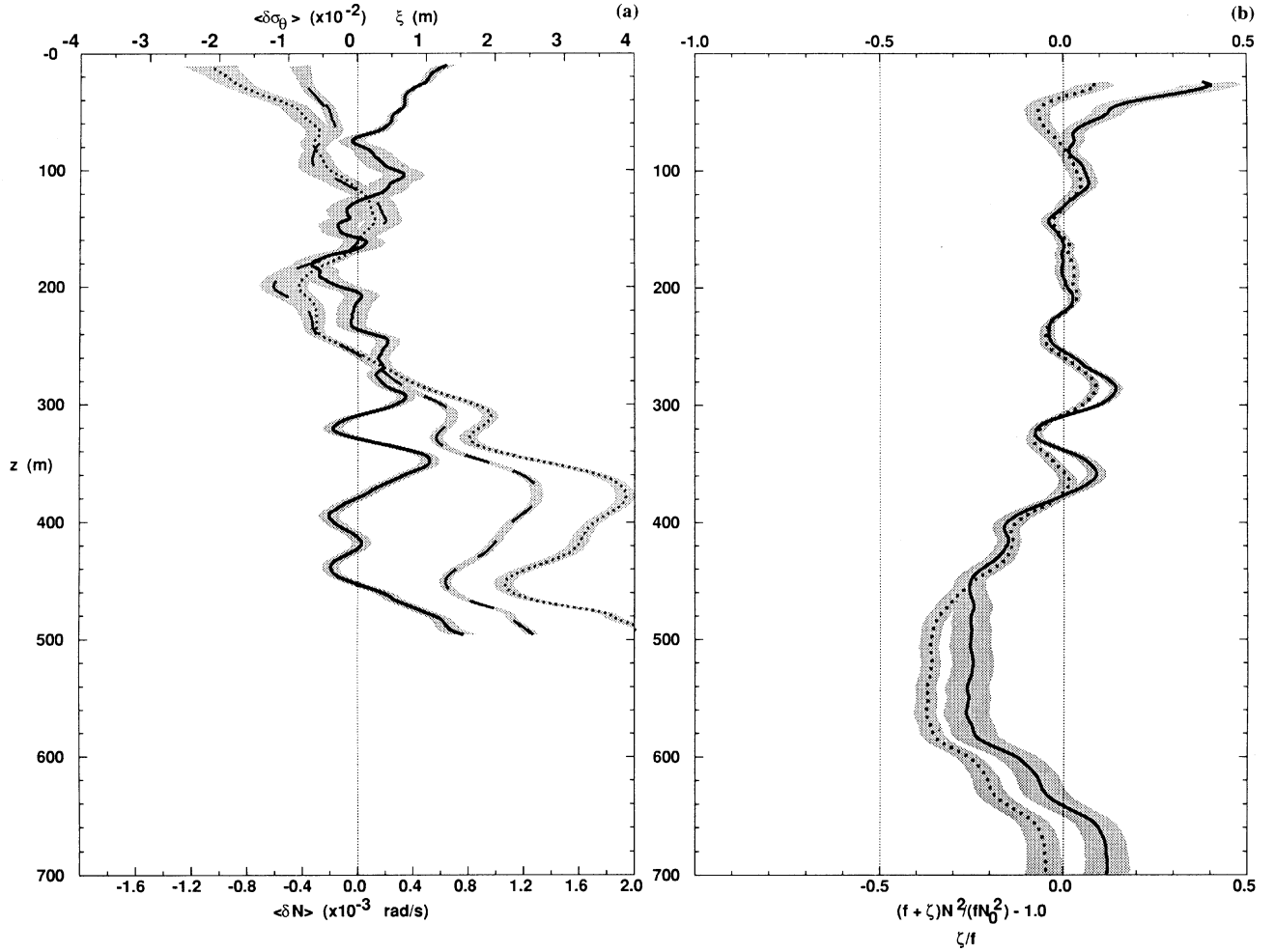


Figure 7. (a) Average HRP density anomaly $\langle \delta \sigma_\theta \rangle$ (dashed), buoyancy frequency anomaly $\langle \delta N \rangle$ (solid), and vertical displacement $\langle \xi \rangle$ (dotted) profiles at site C ($r \sim 1$ km) on the summit plain compared to site F3 ($r = 7.5$ km) on the flanks. The 200-m thick $\langle \delta \sigma_\theta \rangle = 0.02$ density anomaly above the summit plain is too weak to produce a significant buoyancy frequency anomaly. (b) Average profiles of relative vorticity ζ/f (dotted) and potential vorticity anomaly $[(f + \zeta)N^2 - fN_{F_3}^2]/fN_{F_3}^2$ atop the summit plain ($r < 7$ km). The vortex cap has a negative potential vorticity anomaly of $-0.25fN_{F_3}^2$.

$$\int_r^{r_0} \left[\frac{V_\theta^2}{r} + fV_\theta \right] \cdot dr = \delta P = \int_z^{200 \text{ m}} \delta B \cdot dz \quad (4)$$

$$\approx g \frac{\partial \sigma_\theta}{\partial T} \int_z^{200 \text{ m}} \delta T \cdot dz,$$

making use of the hydrostatic balance, $\partial P / \partial z = B$, and the local T , σ_θ -relation, $\partial \sigma_\theta / \partial T$, in the XCP data to infer pressure anomalies δP from the temperature anomalies δT relative to the outermost radial bin at $r \sim 10$ km. The vertical integral is taken from the center of our 150–300 m level of no motion. The effective Coriolis acceleration is evident in the negative anomaly between 400- and 600-m depth (dotted curve in Fig. 8). For radii $r < 4$ km, the pressure anomaly δP in this depth range (solid curve) is of

the same sign and comparable magnitude, so the vortex cap is in cyclogeostrophic balance. At larger radii, the magnitudes of the two sides of (4) remain comparable but the vertical structure differs. The discrepancy becomes even greater below 600-m depth, where a growing negative pressure anomaly has no balancing signal from the effective Coriolis acceleration. This discrepancy is seen independently in both the XCP and HRP data. The horizontal momentum-flux divergences on the righthand side of (3) cannot account for it, making at most a 10% contribution. The vertical momentum-flux divergence contribution might be estimated from $\langle u_r'^2 \rangle$ and the bottom slope

$$\int_r^{r_0} \frac{\partial \langle u_r' w' \rangle}{\partial z} dr = \int_r^{r_0} \frac{\partial (\alpha \langle u_r' \rangle)}{\partial z} dr.$$

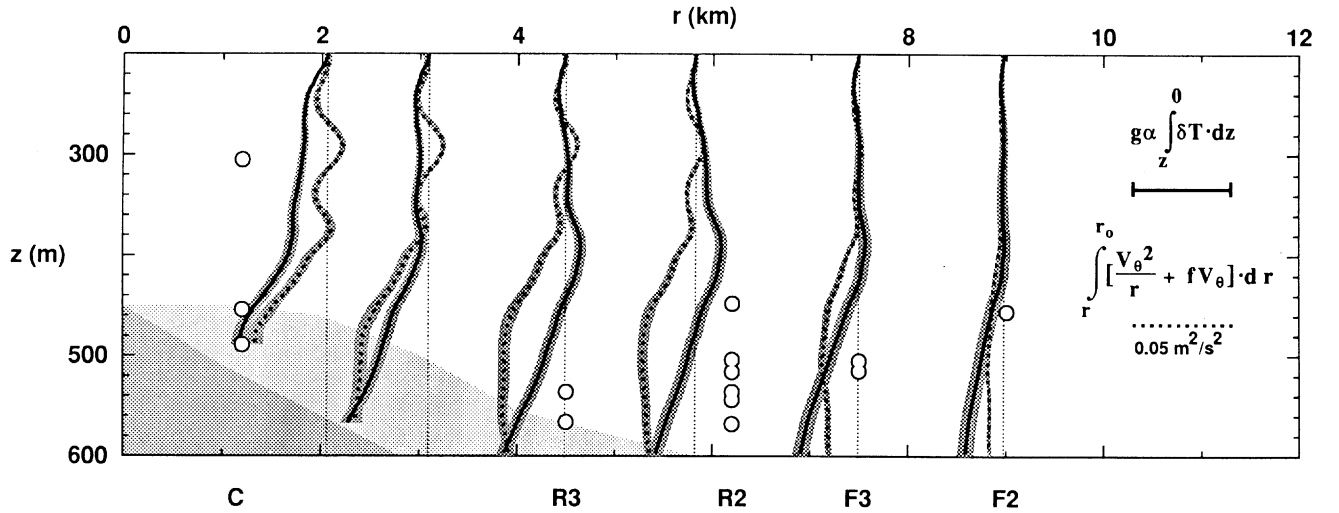


Figure 8. Comparison of the radially-integrated mean effective Coriolis acceleration $\int_r^{r_0} \left[\frac{\langle v_\theta^2 \rangle}{r} + f \langle v_\theta \rangle \right] \cdot dr$ (dotted) with the vertically-integrated buoyancy anomaly $g \frac{\partial \theta}{\partial T} \int_{z_0}^z \langle \delta T \rangle_\theta \cdot dz$ (solid) as a test of the cyclogeostrophic (gradient-wind) balance (3). The quantities are comparable immediately above the summit plain for radii $r < 4$ km; a dome of cold water exists over the summit plain. But the vertically-integrated buoyancy anomaly has a different vertical structure for $r > 4$ km.

Assuming that $\alpha = \alpha_0 \exp[(z - z_b)/(z_b - z_0)]$, where α_0 is the bottom slope on the flanks, z_b the bottom depth, and z_0 the depth of the summit plain, so that α decays toward zero when moving off the bottom on a depth scale comparable to that from the bottom to the summit plain, the vertical momentum-flux divergence is unable to explain the observed discrepancy at $r > 4$ km. Reasonable alternative relations for α yield similar results.

The sole remaining plausible explanation for the discrepancy is that the azimuthal sampling is inadequate to filter out the dipolar horizontal temperature structure of the diurnal wave, $n\theta - \omega t$. At depths below the summit rim over the flanks, there is usually one azimuthal bin with no data points in it. We conclude that the unbalanced pressure anomaly δP at radii $r > 4$ km and depths $z > 500$ m is due to sampling bias.

4.6 Radial Heat Fluxes and Wave Rectification

Brink (1995) also reported a dome of cold water over the summit associated with anticyclonic flow. He argued that an outward radial heat-flux $\langle u_r T' \rangle = 0.4^\circ\text{C cm/s}$ was maintaining the vortex cap against benthic Ekman downwelling $\bar{w} \bar{T}_z$ ($\bar{w} = -0.03$ to -0.13 cm s^{-1} and $\bar{T}_z = (0.7-1.5) \times 10^{-2} \text{ }^\circ\text{C m}^{-1}$) inferred from the near-bottom radial outflow found by Eriksen (1991) and himself. His Ekman term was an order of magnitude larger than his radial heat-flux divergence, which is an order of magnitude larger still than our estimate (Figs. 17 and 18). A possible reason for this discrepancy is that Brink's param-

eterization overestimated the bottom stress. A factor of ten smaller value arises using an eddy viscosity of $10 \times 10^{-4} \text{ m}^2 \text{ s}^{-1}$ as inferred from the turbulent measurements. Over a sloping bottom, MacCready and Rhines (1993) have shown that downslope Ekman transport will set up horizontal pressure gradients which suppress the bottom flow geostrophically, isolating the mean flow and eliminating the bottom stress. In this case, the vortex would become semidetached. There are indications that the azimuthal velocity $\langle v_\theta \rangle_\theta$ and relative vorticity $\langle \zeta \rangle_\theta$ weaken toward the bottom near the summit rim (Figs. 2 and 3). Variable bathymetry is another means by which the bottom stress might be overestimated if the vortex is in contact with the bottom over only a small fraction of its azimuth. But the above arguments do not explain the persistent outward radial velocities observed near the bottom (Eriksen, 1991; Brink, 1995; Freeland, 1994).

Here, we wish to point out some subtleties in the wave rectification problem that hinder inferring balances with incomplete data. Consider steady ($\partial/\partial t = 0$), azimuthally-averaged ($\partial/\partial \theta = 0$) conservation of azimuthal momentum and buoyancy in a tall (or equivalently a vertically-integrated) vortex ($\partial/\partial z \approx 0$)

$$(f + \zeta) \bar{u}_r = - \frac{\partial \langle v'_\theta w' \rangle}{\partial z} \quad (5)$$

$$N^2 \bar{w} = - \frac{1}{r} \frac{\partial [r \langle u'_r b' \rangle]}{\partial r} \quad (6)$$

$$\frac{1}{r} \frac{\partial(r\tilde{u}_r)}{\partial r} + \frac{\partial\tilde{w}}{\partial z} = 0. \quad (7)$$

where $\zeta = V_\theta/r + \partial V_\theta/\partial r$ is the background mean vorticity, b' , u_r' , v_θ' , and w' are the wave buoyancy, radial, azimuthal, and vertical velocities, and \tilde{u}_r and \tilde{w} are *wave-induced mean* flows forming a cross-stream circulation. The $\langle u_r'v_\theta' \rangle$ horizontal momentum-flux vanishes (see Fig. 17), and Brink (1995) showed that $\tilde{u}_r\partial\bar{B}/\partial r$ is negligible. The vertical buoyancy-flux $\langle w'b' \rangle$ due to turbulent mixing, $K_p N^2 \lesssim 2 \times 10^{-8} \text{ m}^2 \text{ s}^{-3}$, could contribute as much as the Ekman downwelling only if confined to vertical scales of 3–10 m, so it will be ignored here. Substituting (5) and (6) into continuity (7), we find that

$$\frac{\langle v_\theta'w' \rangle}{f + \zeta} = -\frac{\langle u_r'b' \rangle}{N^2}, \quad (8)$$

recognizing that the constants of integration are zero for a wave field. As shown in Appendix A, this relation holds exactly for inviscid vortex-trapped waves. Thus, in (5) and (6), wave fluxes can exactly balance wave-induced mean advective fluxes to maintain a steady state independent of the Ekman flow; the background field remains unchanged by the waves' radial heat-flux and vertical momentum-flux unless dissipative processes act to alter their interrelationship. This is a general result for waves propagating in a background mean shear known as the *nonacceleration theorem* (Andrews and McIntyre, 1976; Dunkerton, 1980). If the radial heat-flux arises from a vortex-trapped wave as interpreted here, its role in maintaining the background vortex cannot be evaluated without measurements of the vertical momentum-flux $\langle v_\theta'w' \rangle$. How forced/damped waves affect the mean depends sensitively on the strength and nature of the dissipative processes. For example, in cases where such damping can be parameterized as eddy diffusivities and viscosities, the background diffuses in the vertical or horizontal depending on the eddy Prandtl number (see, e.g., Flierl and Mied, 1985). Our main point here is that, without knowing the detailed nature of the dissipative processes or measuring all the flux-divergences, determination of the rate of change of background quantities is subject to misinterpretation. In the present case, the data do not allow reliable estimation of the vertical momentum-flux $\langle v_\theta'w' \rangle$.

5. The Diurnal Shear Layer

5.1 Temporal Behavior

Current-meter time-series (Genin *et al.*, 1989; Eriksen, 1991; Noble *et al.*, 1994; Brink, 1995) have established that there is a $\pm 15 \text{ cm s}^{-1}$ diurnal oscillation atop the summit plain of Fieberling Guyot with large contributions from both K_1 (0.933f) and O_1 (0.865f) tidal frequencies.

Both are 100 times as energetic as the barotropic tides in the far field, with K_1 being about four times larger than O_1 . Beating of these two tidal constituents produces a subharmonic fortnightly cycle and a harmonic at M_2 ($\delta T = 0.28^\circ\text{C}$). The diurnal frequency is confirmed by the HRP profile time-series at C though the tidal constituents cannot be separated. Grayscale HRP time-series at site C (Fig. 9) reveal clockwise rotation of the velocity vector with time and counterclockwise rotation with depth (downward phase propagation) below 300-m depth. Dropped lag coherences for vertical wavelengths $\lambda_z = 32\text{--}128 \text{ m}$ imply a period of 23.6 h (0.95f), consistent with the current-meter measurements. Similar vertical and temporal phase behavior is observed in the 300- to 600-m depth range of the flank profile time-series, well-isolated from the bottom.

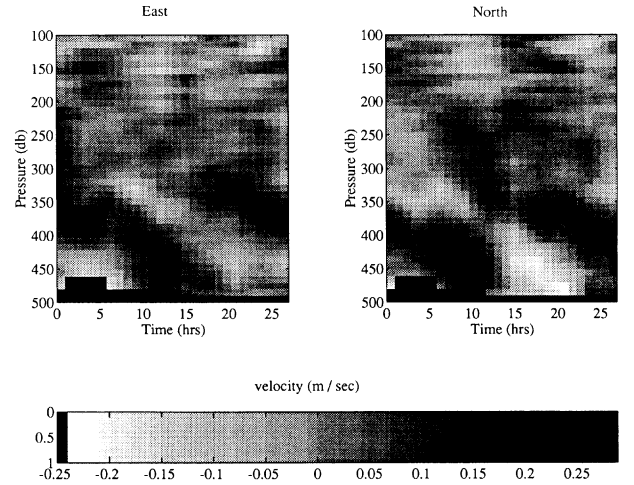


Figure 9. Grayscale plots of east and north velocity from a 27-h long HRP profile time-series at site C on the summit plain. HRP profiles were collected every 3 h. The depth average has been set equal to zero. Larger amplitudes and downward phase propagation are evident below 300-m depth.

Vertical isopycnal excursions of $\pm 20 \text{ m}$ are observed in the center and flank HRP time-series with similar vertical and temporal scales as found in velocity. Their downward phase propagation over the flank leads us to conclude that the steplike structures in the temperature and salinity profiles are produced by the diurnal strain field and not turbulent mixing. At site C on the summit plain, the vertical displacement field is dominated by semidiurnal harmonics.

5.2 Spatial Structure

Azimuthally averaging the east and north velocities in the XCP snapshots filters out axisymmetric flow associated with the vortex and isolates azimuthal-mode-one structure associated with the diurnal oscillations.

Diurnally backrotating the profiles to a common time before averaging did not capture significantly more variance because the XCP profiles were all collected within a few hours of the same phase of the diurnal tidal forcing.

Radial profile sections of azimuthally-averaged, WKB-normalized east and north velocity, $\langle u \rangle_\theta$ and $\langle v \rangle_\theta$, are displayed in Fig. 10. WKB-stretching produces higher vertical resolution where N is small, accounting for the smaller vertical scales at depth than in shallow water. A 150-sm thick layer of intensified shear is evident immediately above the summit plain (550–700 sm, 350–500 m). The signal decays on 3–4 km radial scales away from the summit but is still visible at 10-km radius.

The efficacy of the averaging scheme in isolating the bulk of the variance above the summit plain is demonstrated in Fig. 11. Between 550- and 650-sm depth, the variance in the average (a) greatly exceeds that in the residual (b). At other depths, the residual contains more variance than the average, indicating that azimuthal-mode-one structure dominates only immediately above the summit plain. Maximum velocities exceeding 15 cm s^{-1} lie between 600 and 650 sm (400 and 450 m), $\sim 50 \text{ m}$ above the bottom. Velocity maxima 50 m above the bottom at $\sim 450\text{-m}$ depth are also seen at the rim in the ADCP data (Brink, 1995). This is not consistent with the evanescence away from the bottom expected for seamount-trapped waves.

The relatively low variance in both the average and residual between 150- and 500-sm depth is a consequence of assuming a level of no motion in that depth range. This may also result in excess variance below the summit depth, particularly in the residual (Fig. 11b), so this signal cannot unambiguously be interpreted as due to critical reflection from the flank slopes. Conservatively, the difference between the WKB-normalized residual kinetic energies at 300–550 sm and 700–1200 sm can be thought of as a measure of the uncertainty in the barotropic velocity.

The diurnal shear layer (Fig. 10) is present in both east and north velocities but is out of phase in the vertical in the sense that the velocity vector turns counterclockwise with depth. This can be seen most clearly in Fig. 12, which displays a radial slice of the orientation of the horizontal velocity vector, $\theta = \text{Arctan}(\langle v \rangle_\theta / \langle u \rangle_\theta)$, in the depth range where the signal is most energetic; the orientation θ is a measure of the phase for near-inertial internal gravity waves. It increases monotonically with depth by 240° in 150 sm. This uniform phase gradient $\partial\theta/\partial z (\equiv k_z)$ is consistent with the upward-looking ADCP measurements in the bottom 50 m at R2 (Fig. 1). Brink (1995) reports that the ADCP-measured phase gradient above 550 m (750 sm) is four times greater than in his (1989) seamount-trapped wave model including a time-dependent benthic Ekman layer. The XCP profiles show that this gradient also extends over a depth range four times larger than predicted by his model (Fig. 13). The gradient corre-

sponds to a vertical wavelength $\lambda_z \approx 250 \text{ sm}$. If interpreted as a near-inertial internal wave, the counterclockwise turning with depth implies downward phase and upward energy propagation. The orientation also increases by 30° in 5–7 km radius (Fig. 12). For an internal wave, energy propagates along lines of constant phase in the vertical plane, so this implies outward as well as upward energy propagation.

Vertical wavenumber spectra (Fig. 14) reiterate the rotary character of the signal with depth. The shear layer over the summit plain appears as a peak at vertical wavelength $\lambda_z = 256 \text{ sm}$ in the counterclockwise-with-depth (CCW) spectrum over the summit. The peak is most pronounced in the variance-preserving spectrum. There is no corresponding enhancement in the clockwise-with-depth (CW) spectrum at this wavelength. The CW spectrum is redder ($k_z^{-5/2}$) than the GM model (Garrett and Munk, 1975; Cairns and Williams, 1976) but has comparable levels at lower wavenumbers ($\lambda_z > 50 \text{ sm}$). At radii greater than 10 km, there are no significant peaks in either the CCW or CW spectra. Both have the same spectral slope but slightly lower (0.7) levels than the GM model. Spectral slopes are steeper (k_z^{-3}) for vertical wavelengths $\lambda_z < 50 \text{ sm}$. Clockwise rotation dominates above 500-sm depth (300 m) as is typical of the ocean pycnocline (Leaman and Sanford, 1975).

Figure 15 compares the horizontal structure of the amplitude and phase of the $\lambda_z = 256 \text{ sm}$ CCW component with that of the gravest-mode seamount- and vortex-trapped waves. The observed structure resembles the gravest mode in that the largest amplitudes are found above the summit plain and it exhibits nearly uniform orientation. Moving off the summit plain, the observed vectors become weaker and of more random orientation. Comparing just the radial decay of amplitude, Fig. 16 displays an envelope of solutions for the vortex-trapped near-inertial wave model constrained by the observed buoyancy frequency N , vortex radius r_o , vorticity ζ , and vertical wavelength λ_z (gray stippling). Further constraining the Eulerian frequency to be equal to the K_1 diurnal frequency produces the black envelope of solutions. The seamount-trapped wave model behavior (Δ) better matches the vortex-trapped model behavior than the XCP data (\bullet), but all three show the largest amplitude inside the vortex and decay on scales of a few kilometers outside the vortex. Since the gravest-mode horizontal structure for the two wave models is nearly identical, it cannot be used to identify the dynamics of the diurnal shear layer.

5.3 Radial Heat-Flux

A striking feature in the summit plain current-meter records is the radial heat-flux $\langle u_r T' \rangle$ associated with the diurnal oscillations (Brink, 1995). Johnson and Sanford

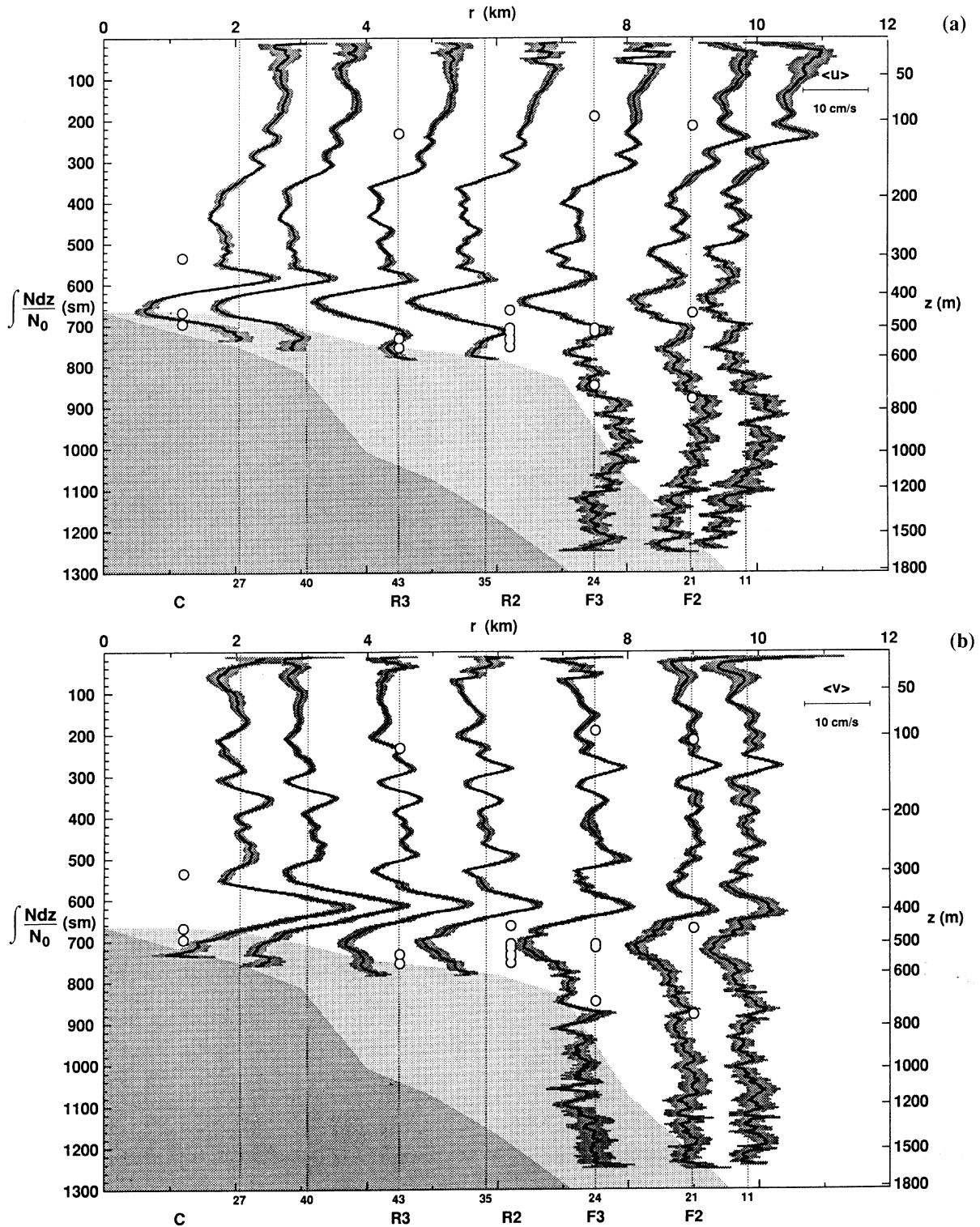


Figure 10. Radial sections of azimuthally-averaged, WKB-normalized east velocity $\langle u \rangle_\theta$ (a) and north velocity $\langle v \rangle_\theta$ (b) over the summit plain and flanks. Shading about the profiles indicates one standard error. WKB-stretched depths are indicated along the left axis and true depths along the right axis. Light and dark silhouettes indicate extremes of bathymetry, open circles the locations of current-meters (Wichman *et al.*, 1993), and numbers at the bottom the number of drops going into each average. A 150-sm thick layer of $10\text{--}15\text{ cm s}^{-1}$ shear lies 50–100 sm above the summit plain and rim, evanesing radially away from the seamount. Extrema in $\langle u \rangle_\theta$ and $\langle v \rangle_\theta$ are not at the same depths but offset in the sense that the velocity vector turns counter-clockwise with depth (see Figs. 12 and 13). There is also a horizontally-coherent wave of $\lambda_z = 50\text{ sm}$ in $\langle v \rangle_\theta$ but not $\langle u \rangle_\theta$ between 200- and 400-sm depth.

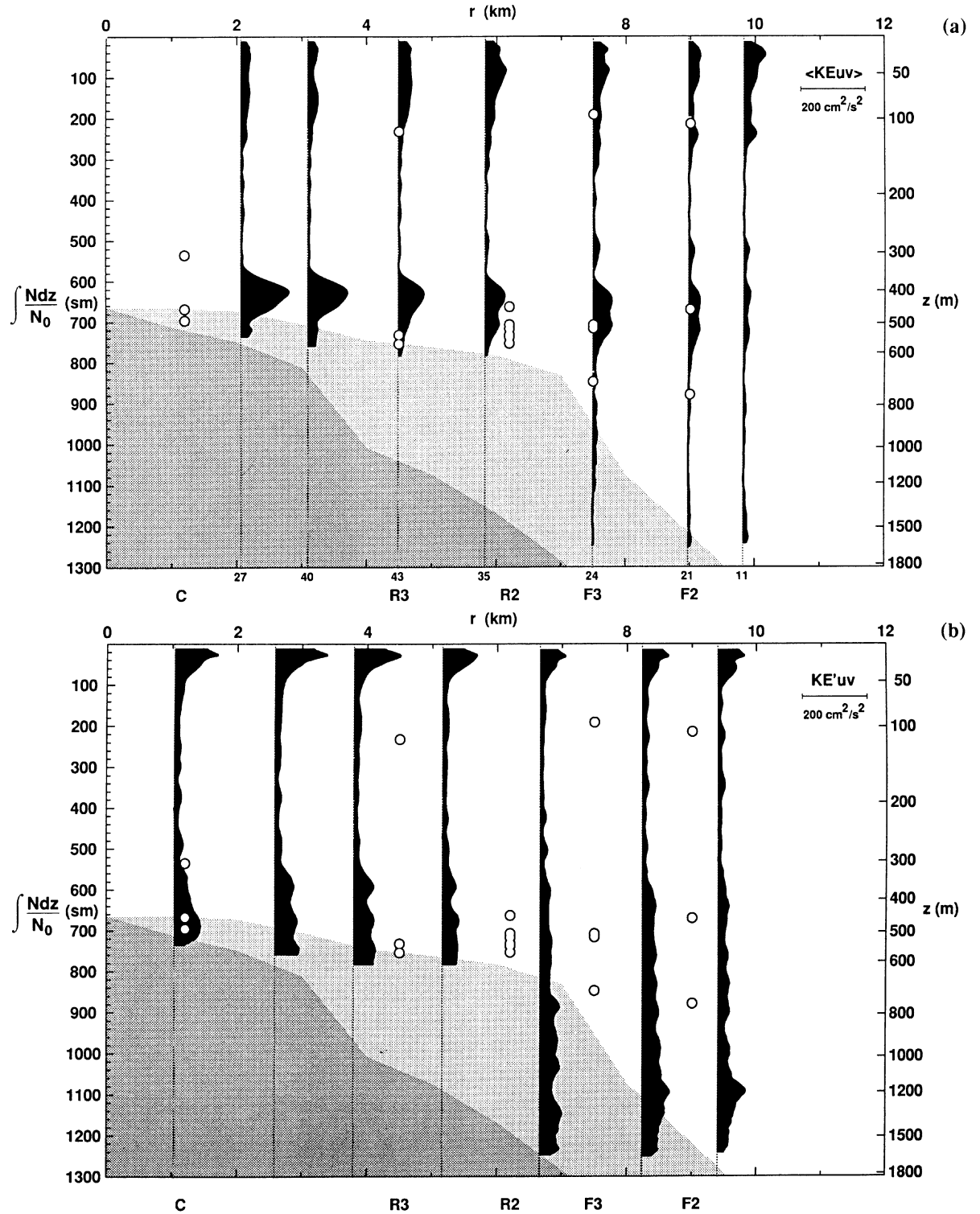


Figure 11. Radial sections of WKB-normalized (a) average Cartesian kinetic energy $\langle KE_{uv} \rangle_\theta = (\langle u \rangle_\theta^2 + \langle v \rangle_\theta^2)/2$ and (b) the residual energy $KE'_{uv} = \langle u'^2 + v'^2 \rangle_\theta/2$. The average kinetic energy (a) has a peak exceeding $100 \text{ cm}^2 \text{ s}^{-2}$ between 600 and 700 sm (400–500 m depth), 50–100 sm above the summit plain. This peak corresponds to the 150-m thick shear layer in Fig. 10. The residual kinetic energy (b) has more uniform overall energies with no well-pronounced peak above the summit, demonstrating the efficacy of the averaging scheme in isolating the feature over the summit plain. The larger residual energy below 500-sm depth is due to removal of 150–500 sm velocities from the profiles before averaging.

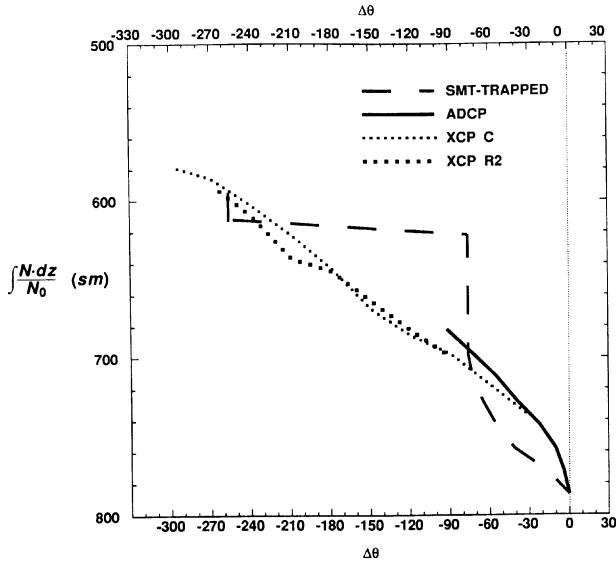


Figure 13. Comparison of the velocity orientation $\Delta\theta$ as a function of WKB-stretched depth from Brink's (1990) seamount-trapped wave model (dashed), the rim R2 ADCP mooring (solid), and XCPs near the center and on the rim of the summit plain (dotted). XCP and ADCP gradients are roughly consistent in the overlapping depth range 680–780 m. The model's time-dependent bottom Ekman spiral is also roughly consistent with the turning in this depth range. However, the XCP profiles indicate that the phase gradient θ_z extends to 580-sm depth while the seamount-trapped wave model indicates uniform phases above 700 sm until 620-sm depth, then a 180° phase shift (velocity reversal) at shallower depths.

plain than at similar depths 10 km away (Fig. 19). Patches of high energy turbulent dissipation are well-correlated with the sites of Froude number (not shown). Error bars are 97% confidence limits computed using the bootstrap technique (Efron and Gong, 1983) and do not differ significantly from those computed assuming a log-normal distribution (Baker and Gibson, 1987).

The average kinetic energy dissipation rate ϵ above the summit plain is $(3.3 \pm 0.1) \times 10^{-8} \text{ W kg}^{-1}$, sufficient to drain the total energy in the diurnal oscillation ($\sim 5.0 \times 10^{-3} \text{ m}^2 \text{ s}^{-2}$) and vortex cap ($\sim 2.5 \times 10^{-3} \text{ m}^2 \text{ s}^{-2}$) in 3 days. For comparison, the amount of time it would take open-ocean turbulence to deplete a Garrett-and-Munk internal wave field is 100 days. The short depletion time over Fieberling Seamount implies that barotropic diurnal tides are continuously supplying energy to these motions on a similar timescale to maintain the observed signals. The issue of intensified near-bottom turbulence contributing little mixing because it acts in an unstratified benthic boundary layer (Garrett, 1990) is not germane above either the summit plain or the flanks (Toole *et al.*, 1995) where strong turbulence is found in the stratified waters.

The diapycnal eddy diffusivities inferred from the microstructure data ($K_T = \chi_T / (2\bar{T}_z^2)$, Osborn and Cox, 1972;

$K_p \leq 0.25\epsilon/\bar{N}^2$, Osborn, 1980) have a typical open-ocean value of $0.1 \times 10^{-4} \text{ m}^2 \text{ s}^{-1}$ above 300-m depth (Fig. 20). In the 200-m thick layer atop the summit plain, they approach $50 \times 10^{-4} \text{ m}^2 \text{ s}^{-1}$ (excluding diffusivities within 10 m of the bottom that could be in a bottom boundary layer). The steady Ekman scale height for an effective eddy viscosity of $50 \times 10^{-4} \text{ m}^2 \text{ s}^{-1}$ is 8 m. Similar eddy diffusivities ($100 \times 10^{-4} \text{ m}^2 \text{ s}^{-1}$) were found by Mudge (1994) at Cobb Seamount. In his case, the largest values were near the rim depth and extended outward several seamount radii. Nabatov and Ozmidov (1988) found numerous 10-m thick patches above and in detached layers in the vicinity of Josephine and Ampere seamounts with turbulent dissipation rates of $(6.0\text{--}400.0) \times 10^{-7} \text{ W kg}^{-1}$. Osborn (1978) reported average dissipation rates of $10^{-8} \text{ W kg}^{-1}$ within 5–80 km of an island, corresponding to eddy diffusivities of $10^{-4} \text{ m}^2 \text{ s}^{-1}$, but these measurements were not proximal to the topography and the turbulence may have been due to a recent storm passage. Toole *et al.* (1995) and Eriksen (1995) find eddy diffusivities of $(2.0\text{--}6.0) \times 10^{-4} \text{ m}^2 \text{ s}^{-1}$ in the stratified boundary layer above the flanks of Fieberling.

Averaged over the ocean basin, these diffusivities are at most equivalent to the $0.1 \times 10^{-4} \text{ m}^2 \text{ s}^{-1}$ observed in the main pycnocline (Moum and Osborn, 1986; Gregg, 1989; Ledwell *et al.*, 1993; Toole *et al.*, 1994; Polzin *et al.*, 1995), so seamount mixing cannot raise basin-average mixing levels to a vertical advection-diffusion balance (Munk, 1966) value of $10^{-4} \text{ m}^2 \text{ s}^{-1}$.

7. Summary and Discussion

Fine- and microstructure profiles collected over Fieberling Seamount reveal a 200-m thick layer of intense activity overlying the summit plain. In this layer there coexists (i) an anticyclonic vortex cap of relative vorticity $-0.5f$ (Fig. 2b), (ii) a slightly subinertial diurnal shear layer (Figs. 9 and 10), and (iii) intensified turbulence with average dissipation rates $\epsilon = 3.3 \times 10^{-8} \text{ W kg}^{-1}$ (Fig. 19) and eddy diffusivities $K_p = 10 \times 10^{-4} \text{ m}^2 \text{ s}^{-1}$ (Fig. 20). All these motions appear to be ultimately driven by the barotropic K_1 and O_1 diurnal tides. The turbulence levels imply decay times of ~ 3 days, so it is clear that the barotropic tides are continually pumping energy into the summit motions.

The vortex was in cyclogeostrophic balance, at least inside $r = 4 \text{ km}$ (Fig. 8). At larger radii and depths greater than 600 m, the radial pressure gradient and effective Coriolis acceleration do not balance. This imbalance could not be explained by a contribution from momentum-flux divergences. It appears to be the result of inadequate azimuthal sampling. The strength of the vortex exhibited a fortnightly cycle with peak-to-peak variations of $-0.4f$ to $-0.5f$ (Fig. 6), evidence that it was at least partially driven by the diurnal tides. Other evidence that the

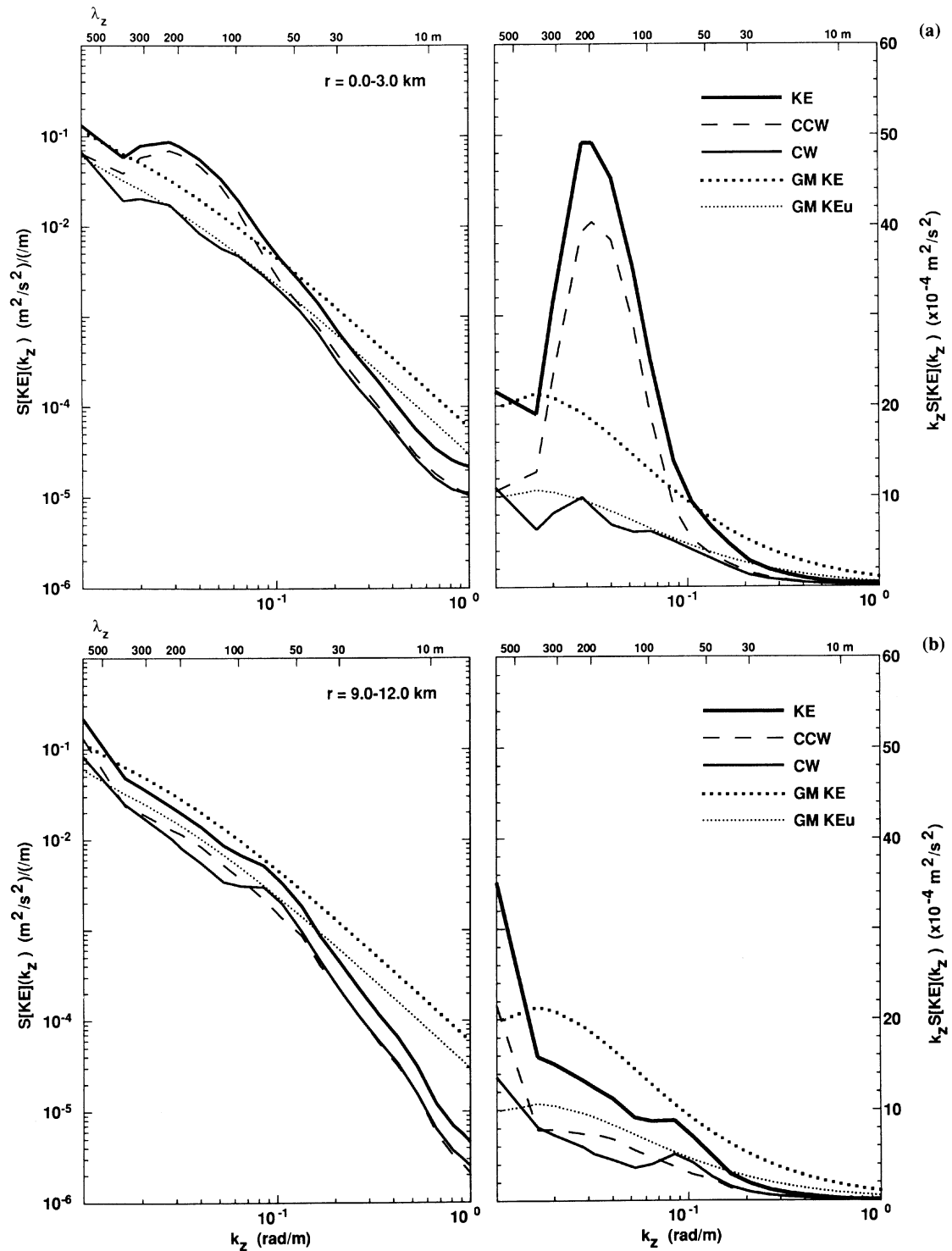


Figure 14. Rotary vertical wavenumber spectra of kinetic energy for drops at 0–3 km (upper two panels) and 9–12 km radius (lower two panels). Spectra are presented in both log-log (left panels) and variance-preserving (right panels) formats. The 0–3 km spectra emphasize the depth-rotary nature of the shear-layer signal above the summit plain. They are dominated by a counterclockwise-with-depth (CCW) peak at $\lambda_z = 256$ m. There is no corresponding enhancement of CW energy. Away from the seamount, clockwise and counterclockwise spectra are similar and slightly below GM model levels.

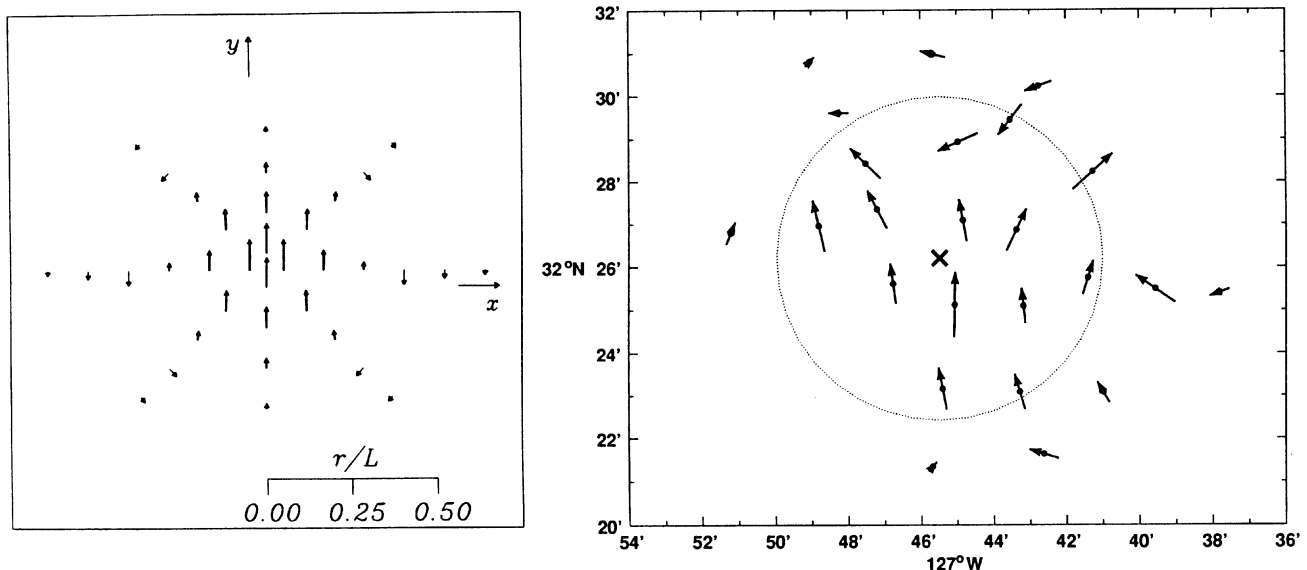


Figure 15. Horizontal structure for lowest-mode seamount- or vortex-trapped wave (left panel; after Brink, 1989), and the amplitude and phase of the observed $\lambda_z = 256$ m counterclockwise-with-depth signal (right panel). The seamount- and vortex-trapped wave have identical horizontal structure. The observations have been averaged in $2' \times 2'$ bins. Over the summit plain, the signal is strongest and has nearly uniform orientation. Off the summit, amplitudes are weaker and orientation more random.

vortex cap could not be explained with inviscid Taylor cap dynamics is that its core contained a negative potential vorticity anomaly (Fig. 7) while Taylor cap dynamics conserve potential vorticity. Wave rectification of the diurnal tides is the most likely mechanism for maintaining the cold dome of the vortex against benthic Ekman decay. An outward radial heat-flux $\langle u_r T \rangle$ is associated with the diurnal shear layer but, without measurements of the vertical momentum-flux $\langle v_\theta w' \rangle$, the role that the diurnal oscillation plays in driving the vortex cannot be evaluated rigorously. The vortex strength also changed dramatically every few months for reasons that were unclear but may be related to changes in the direction of the impinging background flow (Brink, 1995).

The diurnal shear layer also displays a fortnightly modulation of the K_1 beating against the O_1 tide. Its jet-like azimuthal-mode-one horizontal structure rotates clockwise with time and counterclockwise with depth ($\lambda_z = 250$ m). Its slightly subinertial frequency (Fig. 9) and horizontal structure (Figs. 15 and 16) closely resemble those of a seamount-trapped topographic wave (Brink, 1989, 1990). However, a vortex-trapped near-inertial internal wave has similar properties (Kunze *et al.*, 1995). Moreover, the maximum variance being 50 m above the bottom, the continuous counterclockwise turning of the velocity vector with depth (Figs. 12 and 13), and the radial heat-flux (Figs. 17 and 18) more closely resemble a vortex-trapped than a seamount-trapped wave.

We conclude that the diurnal shear layer observed in the HRP and XCP measurements is a vortex-trapped internal wave forced by the barotropic tide impinging on the seamount summit, its subinertial frequency being allowed

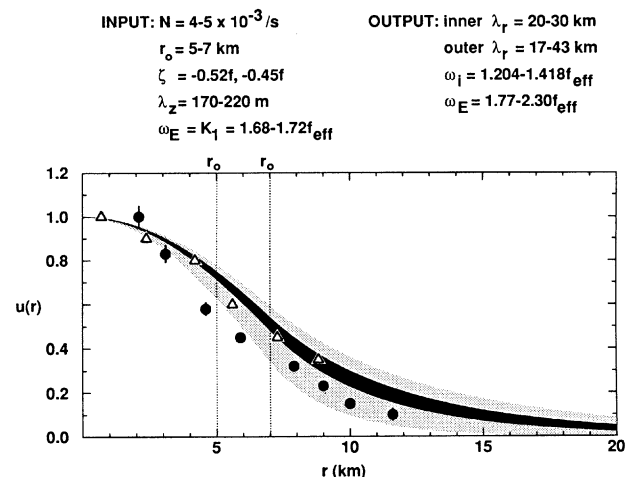


Figure 16. Radial structure of horizontal velocity for a vortex-trapped mode (stippled envelope) constrained by the observed range of buoyancy frequency N , core vorticity ζ , core radius r_o and vertical wavelength λ_z . If further constrained to have the observed K_1 diurnal Eulerian frequency, only the solid envelope results, corresponding to an inner radial wavelength of 27 km and an outer (decay) radial wavelength $\lambda_\theta = 25$ km. A seamount-trapped wave has identical radial structure (Δ). XCP observations (\dagger) lie near the model curves.

by the strong negative vorticity of the vortex cap. If this interpretation is correct, then, for deep seamounts where the only significant slightly subinertial forcing is the barotropic tides, this phenomenology will be found only just poleward of 30° . Equatorward of 30° , diurnal frequencies can propagate as free internal waves and thus will not be trapped. Much poleward of 30° , a vortex cap

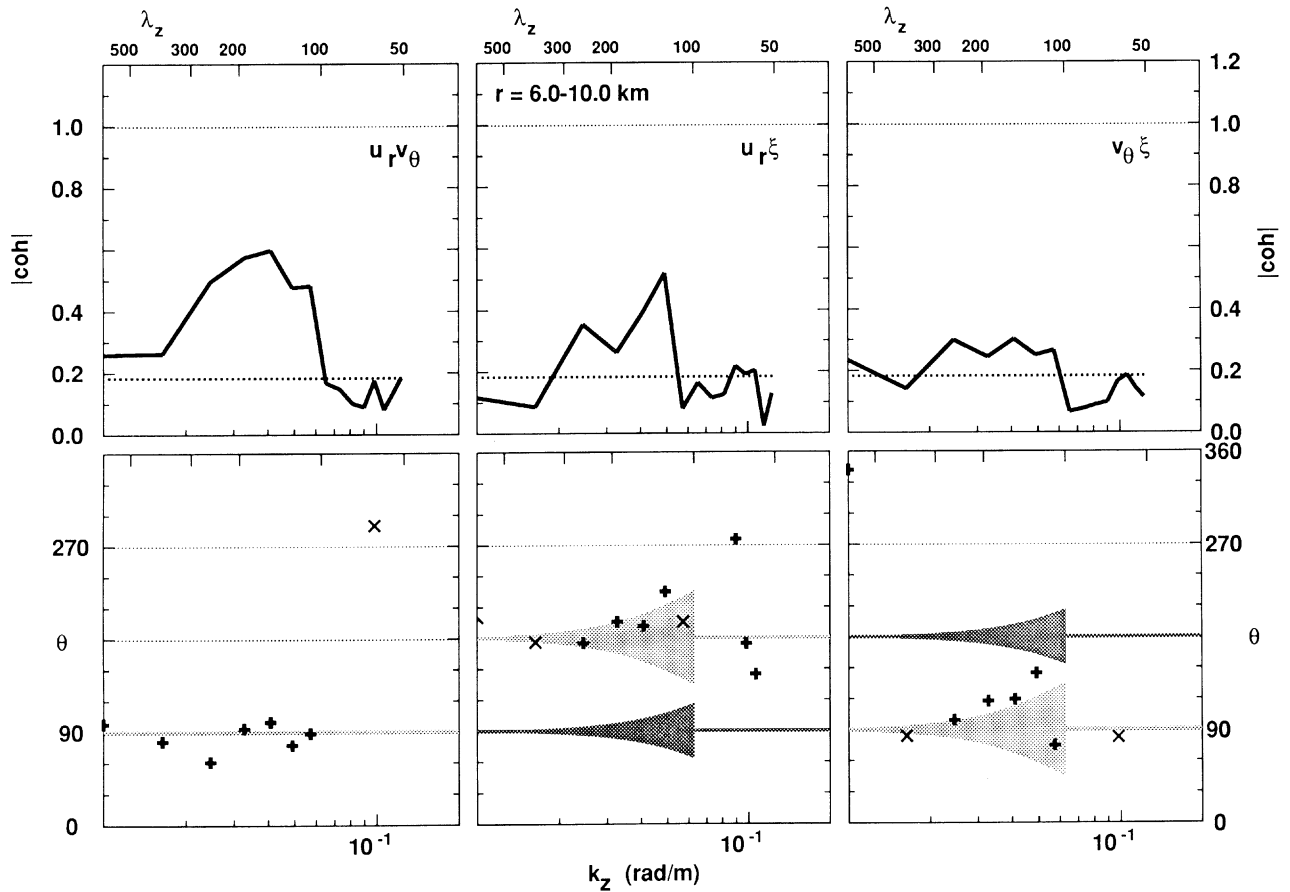


Figure 17. Coherence magnitude (upper panels) and phase (lower panels) as a function of vertical wavenumber for XCP and HRP profiles at radius $r = 6\text{--}10$ km. Phase relations for vortex- and seamount-trapped waves are shown by the light and dark stippling, respectively. The spreading of the phase relations by an eddy viscosity $\nu_e \leq 100 \times 10^{-4} \text{ m}^2 \text{ s}^{-1}$ (Appendices B and C) is shown for $\lambda_z > 100$ m. Coherence is significant for vertical wavelengths $\lambda_z = 100\text{--}300$ m. In this band, radial and azimuthal velocities are 90° out of phase (consistent with the CCW turning with depth), radial velocity u_r' and vertical displacement ξ' 180° out of phase (corresponding to an outward radial heat-flux), and azimuthal velocity v_θ' and vertical displacement ξ' 90° out of phase. These last two phase relations are consistent with vortex-trapped waves propagating upward and clockwise around the seamount, but not with seamount-trapped waves.

will not be strong enough to allow a free diurnal wave in its confines or, equivalently, the vertical wavelength of an allowed vortex-trapped wave (2) would be so small that its amplitude would be undetectable. These restrictions may not apply to shallow seamounts, where broadband atmospheric forcing includes slightly subinertial frequencies that will be resonant with vortex-trapped waves. Given the intermittency of atmospheric forcing and the short decay times of the observed wave, vortex-trapped waves may appear only during forcing. The above is consistent with Codiga's (1995) finding of a diurnal seamount-trapped wave atop shallow Cobb Seamount at $46^\circ 45'\text{N}$.

Elevated turbulence levels of $\varepsilon \approx 10^{-7} \text{ W kg}^{-1}$ are found coincident with the vortex cap and the diurnal oscillation, corresponding to eddy diffusivities of $10 \times 10^{-4} \text{ m}^2 \text{ s}^{-1}$. This is not sufficiently enhanced for seamounts to

play a dominant role in global mixing of the pycnocline, in particular, for them to account for an average eddy diffusivity of $10^{-4} \text{ m}^2 \text{ s}^{-1}$ inferred from a diapycnal advection-diffusion balance (Munk, 1966). With the mixing not occurring in the ocean interior or at lateral boundaries, the surface seems the most likely site of diapycnal mixing for the ocean.

Acknowledgments. We thank Charlie Eriksen and Ken Brink for making their moored current-meter data available to other Fieberling Seamount investigators. Valuable insights into seamount-trapped waves were provided by Ken Brink and Dan Codiga. The HRP data were collected and analyzed under ONR contract N00014-89-J-1073. The XCP data were collected under ONR contract N00014-90-J-1535 and analyzed under contracts N00014-90-J-1535 and N00014-94-I-0038.

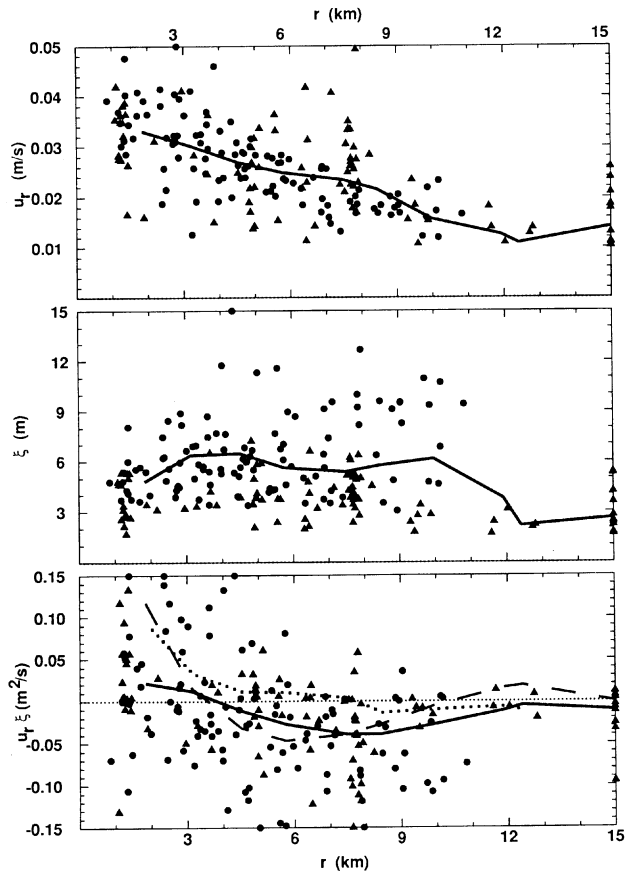


Figure 18. Radial structure of rms radial velocity u_r' (a), rms vertical displacement ξ' (b) and the real (co-spectral) part of the radial displacement flux $u_r'\xi'$ (c) in the $\lambda_z = 100\text{--}300$ m band. Dots and triangles correspond to values from individual XCPs and HRP, respectively. Solid curves are radially-smoothed values. The dotted curve in the $u_r'\xi'$ panel depicts a vortex-trapped wave model prediction given the rms u_r' radial structure, the dashed line uses the rms u_r' inside 1-km radius and the vortex-trapped wave model structure.

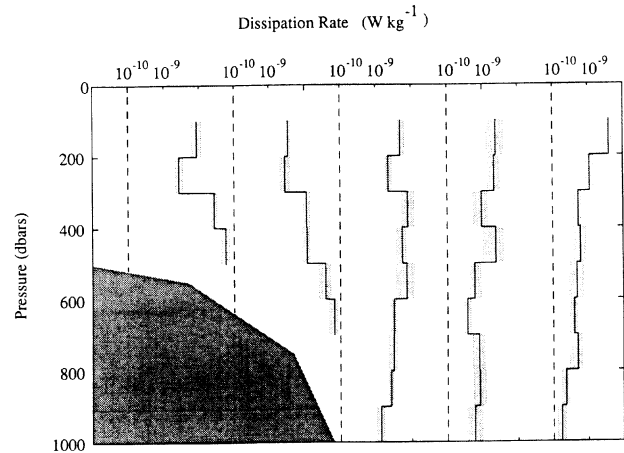


Figure 19. Average kinetic energy dissipation rate ϵ (W kg^{-1}) as a function of depth and radial distance from seamount center with 97% bootstrap confidence limits. Averages are in 100-m thick depth bins, and radial bins over the summit plain, about the rim, the 1500-m isobath, the 2500-m isobath and > 10 km from the seamount center.

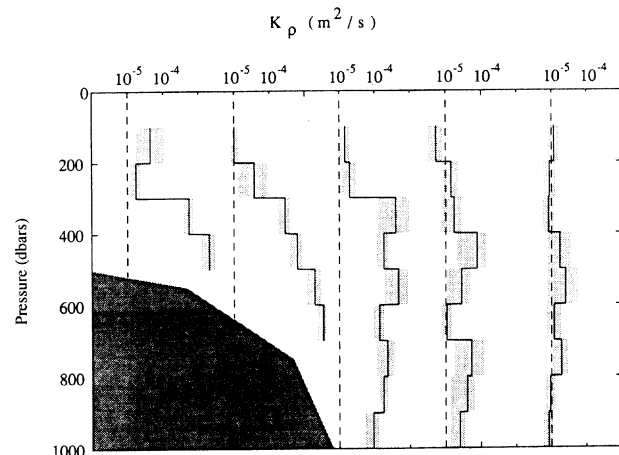


Figure 20. Average turbulent eddy diffusivity K_p ($\text{m}^2 \text{s}^{-1}$) inferred from the kinetic energy dissipation rate ϵ (Fig. 19) as a function of depth and radius. Error bars are 97% confidence limits determined with bootstrap methods. A mixing efficiency of 0.25 is assumed (Oakey, 1982).

References

- Andrews, D.G., and M.E. McIntyre, 1976: Planetary waves in horizontal and vertical shear: The generalized Eliassen-Palm relation and the mean zonal acceleration, *J. Atmos. Sci.*, 33, 2049–2053.
- Baines, P., 1971: The reflection of internal/inertial waves from bumpy surfaces, Part 1, *J. Fluid Mech.*, 46, 273–291.
- Baker, M.A., and C.H. Gibson, 1987: Sampling turbulence in the stratified ocean: Statistical consequences of strong intermittency, *J. Phys. Oceanogr.*, 17, 1817–1836.
- Bell, T.H., 1975: Topographically generated internal waves in the open ocean, *J. Geophys. Res.*, 80, 320–327.
- Boyer, D.L., and X. Zhang, 1990: Motion of oscillatory currents past isolated topography, *J. Phys. Oceanogr.*, 20, 1425–1448.
- Brink, K.H., 1989: The effect of stratification on seamount-trapped waves, *Deep-Sea Res.*, 36, 825–844.
- Brink, K.H., 1990: On the generation of seamount-trapped waves, *Deep-Sea Res.*, 37, 1569–1582.
- Brink, K.H., 1995: Tidal and lower frequency currents above Fieberling Guyot, *J. Geophys. Res.*, submitted.
- Cairns, J.L., and G.O. Williams, 1976: Internal wave observations from a midwater float, 2, *J. Geophys. Res.*, 81, 1943–1950.
- Chapman, D.C., 1989: Enhanced subinertial diurnal tides over isolated topographic features, *Deep-Sea Res.*, 36, 815–824.
- Chapman, D.C., and D.B. Haidvogel, 1992: Formation of Taylor caps over a tall isolated seamount in a stratified ocean, *Geophys. Astrophys. Fluid Dyn.*, 64, 31–65.
- Codiga, D.L., 1991: Fitting Fieberling Guyot, *TopoNews*, Newsletter of ONR Accelerated Research Initiative Flow Over Abrupt Topography, 4, 14–15.
- Codiga, D.L., 1993: Laboratory realizations of stratified seamount-trapped waves, *J. Phys. Oceanogr.*, 23, 2053–2071.
- Codiga, D.L., 1995: ADCP and CTD observations at Cobb Seamount: Low-frequency circulation and amplified subinertial tidal currents, Ph.D. thesis, University of Washington, 92 pp.
- Dunkerton, T.J., 1980: A Lagrangian-mean theory of wave/mean flow interaction with applications to nonacceleration and its breakdown, *Rev. Geophys. Space Phys.*, 18, 387–400.
- Efron, B., and G. Gong, 1983: A leisurely look at the bootstrap, the jackknife and cross-validation, *Amer. Stat.*, 37, 36–48.
- Eriksen, C.C., 1982: Observations of internal wave reflection off sloping bottoms, *J. Geophys. Res.*, 87, 525–538.
- Eriksen, C.C., 1985: Implications of ocean bottom reflection for internal wave spectra and mixing, *J. Phys. Oceanogr.*, 15, 1145–1156.
- Eriksen, C.C., 1991: Observations of amplified flows atop a large seamount, *J. Geophys. Res.*, 96, 15,227–15,236.
- Eriksen, C.C., 1995: Internal wave reflection and mixing at Fieberling Guyot, *J. Geophys. Res.*, submitted.
- Ertel, H., 1942: Ein neuer hydrodynamischer Wirbelsatz, *Meteorol. Z.*, 59, 277–281.
- Flierl, G.R., and R.P. Mied, 1985: Frictionally induced circulations and spin-down of a warm-core ring, *J. Geophys. Res.*, 90, 8917–8927.
- Freeland, H., 1994: Ocean circulation at and near Cobb Seamount, *Deep-Sea Res.*, 41, 1715–1732.
- Garrett, C., 1990: The role of secondary circulation in boundary mixing, *J. Geophys. Res.*, 95, 989–993.
- Garrett, C.J.R., and W.H. Munk, 1975: Space-time scales of internal waves: A progress report, *J. Geophys. Res.*, 80, 291–297.
- Genin, A., P.K. Dayton, P.F. Lonsdale and F.N. Spiess, 1986: Corals on seamount peaks provide evidence of current acceleration over deep-sea topography, *Nature*, 322, 59–61.
- Genin, A., M. Noble and P.F. Lonsdale, 1989: Tidal currents and anticyclonic motions on two North Pacific seamounts, *Deep-Sea Res.*, 36, 1803–1815.
- Genin, A., C.K. Paull and W.P. Dillon, 1992: Anomalous abundances of deep-sea fauna on a rocky bottom exposed to strong currents, *Deep-Sea Res.*, 39, 293–302.
- Gilbert, D., and C. Garrett, 1989: Implications for ocean mixing of internal wave scattering off irregular topography, *J. Phys. Oceanogr.*, 19, 1716–1729.
- Gregg, M.C., 1989: Scaling turbulent dissipation in the thermocline, *J. Geophys. Res.*, 94, 9686–9698.
- Haidvogel, D.B., A. Beckmann, D.C. Chapman and R.-Q. Lin, 1993: Numerical simulation of flow around a tall isolated seamount, Part II: Resonant generation of trapped waves, *J. Phys. Oceanogr.*, 23, 2373–2391.
- Haynes, P.H., and M.E. McIntyre, 1987: On the evolution of vorticity and potential vorticity in the presence of diabatic heating and frictional or other forces, *J. Atmos. Sci.*, 44, 828–841.
- Hogg, N.G., 1973: On the stratified Taylor column, *J. Fluid Mech.*, 58, 517–537.
- Hunkins, K., 1986: Anomalous diurnal tidal currents on the Yermak Plateau, *J. Mar. Res.*, 44, 51–69.
- Huthnance, J.M., 1974: On the diurnal tidal currents over Rockall Bank, *Deep-Sea Res.*, 21, 23–35.
- Huthnance, J.M., 1978: On coastal-trapped waves: Analysis and numerical calculation by inverse iteration, *J. Phys. Oceanogr.*, 8, 74–92.
- Johnson, C.L., and T.B. Sanford, 1980: Anomalous behavior of internal gravity waves near Bermuda, *J. Phys. Oceanogr.*, 10, 2021–2034.
- Kowalik, Z., 1994: Modeling of topographically amplified diurnal tides in the Nordic seas, *J. Phys. Oceanogr.*, 24, 1717–1731.
- Kunze, E., 1985: Near-inertial wave propagation in geostrophic shear, *J. Phys. Oceanogr.*, 15, 544–565.
- Kunze, E., 1986: The mean and near-inertial velocity fields in a warm-core ring, *J. Phys. Oceanogr.*, 16, 1444–1461.
- Kunze, E., and T.B. Sanford, 1986: Near-inertial wave interactions with mean flow and bottom topography near Caryn Seamount, *J. Phys. Oceanogr.*, 16, 109–120.
- Kunze, E., M.A. Kennelly and T.B. Sanford, 1992: The depth dependence of shear finestructure off Point Arena and near Pioneer Seamount, *J. Phys. Oceanogr.*, 22, 29–41.
- Kunze, E., and T.B. Sanford, 1993: Submesoscale dynamics near a seamount. Part I: Measurements of Ertel vorticity, *J. Phys. Oceanogr.*, 23, 2567–2588.
- Kunze, E., R.W. Schmitt and J.M. Toole, 1995: The energy balance in a warm-core ring's near-inertial critical layer, *J. Phys. Oceanogr.*, 25, 942–957.

- Leaman, K.D., and T.B. Sanford, 1975: Vertical energy propagation of inertial waves: A vector spectral analysis of velocity profiles, *J. Geophys. Res.*, 80, 1975–1978.
- Ledwell, J.R., A.J. Watson and C.S. Law, 1993: Evidence of slow mixing across the pycnocline from an open-ocean tracer-release experiment, *Nature*, 364, 701–703.
- LeBlond, P.H., 1966: On the damping of internal gravity waves in a continuously stratified ocean, *J. Fluid Mech.*, 25, 121–142.
- Loder, J.H., 1980: Topographic rectification on the sides of Georges Bank, *J. Phys. Oceanogr.*, 10, 1399–1416.
- Maas, L.R.M., and J.J.M. van Haren, 1987: Observations on the vertical structure of tidal and inertial currents in the central North Sea, *J. Mar. Res.*, 45, 293–318.
- Maas, L.R.M., and J.T.F. Zimmerman, 1989a: Tide-topography interactions in a stratified shelf sea. I. Basic equations for quasi-nonlinear internal tides, *Geophys. Astrophys. Fluid Dyn.*, 45, 1–35.
- Maas, L.R.M., and J.T.F. Zimmerman, 1989b: Tide-topography interactions in a stratified shelf sea, II. Bottom-trapped internal tides and baroclinic residual currents, *Geophys. Astrophys. Fluid Dyn.*, 45, 37–69.
- MacCready, P., and P.B. Rhines, 1993: Slippery bottom boundary layers on a slope, *J. Phys. Oceanogr.*, 23, 5–22.
- McCartney, M., 1975: Inertial Taylor columns on a beta-plane, *J. Fluid Mech.*, 68, 71–95.
- Montgomery, E.T., and J.M. Toole, 1993: Fine- and microstructure observations at Fieberling Guyot: R/V New Horizon Cruise Report, Woods Hole Oceanogr. Inst. Tech. Rpt. WHOI-93-15, 27 pp.
- Moum, J.N., and T.R. Osborn, 1986: Mixing in the main thermocline, *J. Phys. Oceanogr.*, 16, 1250–1259.
- Mudge, T.D., 1994: Mixing around a shallow seamount, Masters thesis, University of Victoria, Victoria, B.C., Canada, 126 pp.
- Müller, P., and N. Xu, 1992: Scattering of oceanic internal gravity waves off random bottom topography, *J. Phys. Oceanogr.*, 22, 474–488.
- Munk, W., 1966: Abyssal recipes, *Deep-Sea Res.*, 13, 707–730.
- Nabatov, V.N., and R.V. Ozmidov, 1988: Study of turbulence above seamounts in the Atlantic Ocean, *Oceanology*, 28, 161–166.
- Noble, M., D.A. Cacchione and W.C. Schwab, 1988: Observations of strong mid-Pacific internal tides above Horizon Guyot, *J. Phys. Oceanogr.*, 18, 1300–1306.
- Noble, M., and L.S. Mullineaux, 1989: Internal tidal currents over the summit of Cross Seamount, *Deep-Sea Res.*, 36, 1791–1802.
- Noble, M.A., K.H. Brink and C.C. Eriksen, 1994: Diurnal-period currents trapped above Fieberling Guyot: Observed characteristics and model comparisons, *Deep-Sea Res.*, 41, 643–658.
- Oakey, N.S., 1982: Determination of the rate of dissipation of turbulent energy from simultaneous temperature and velocity shear microstructure measurements, *J. Phys. Oceanogr.*, 12, 256–271.
- Osborn, T.R., 1978: Measurements of energy dissipation adjacent to an island, *J. Geophys. Res.*, 83, 2939–2957.
- Osborn, T.R., 1980: Estimates of the local rate of vertical diffusion from dissipation measurements, *J. Phys. Oceanogr.*, 10, 83–89.
- Osborn, T.R., and C.S. Cox, 1972: Oceanic finestructure, *Geophys. Fluid Dyn.*, 3, 321–345.
- Padman, L., A.J. Plueddemann, R.D. Muench and R. Pinkel, 1992: Diurnal tides near the Yermak Plateau, *J. Geophys. Res.*, 97, 12,639–12,652.
- Phillips, O.M., 1977: *The Dynamics of the Upper Ocean*, Cambridge University Press, Cambridge, 336 pp.
- Polzin, K.L., 1992: Observations of turbulence, internal waves and background flows: An inquiry into the relationships between scales of motion, Ph.D. thesis, WHOI Tech. Rpt. 93-39, 244 pp.
- Polzin, K.L., J.M. Toole and R.W. Schmitt, 1995: Finescale parameterizations of turbulent dissipation, *J. Phys. Oceanogr.*, 25, 306–328.
- Rhines, P., 1969: Slow oscillations in an ocean of varying depth, Part I. Abrupt topography, *J. Fluid Mech.*, 37, 161–189.
- Rhines, P., 1970: Edge-, bottom- and Rossby waves in a rotating stratified fluid, *Geophys. Fluid Dyn.*, 1, 273–302.
- Roden, G.I., 1987: Effect of seamount and seamount chains on ocean circulation and thermohaline structure, *Seamounts, Islands and Atolls*, B.H. Keating, P. Fryer, R. Batiza, and G.W. Boehlert, (eds.), AGU, Washington, DC, pp. 335–354.
- Roden, G.I., 1991: Mesoscale flow and thermohaline structure around Fieberling Seamount, *J. Geophys. Res.*, 96, 16,653–16,672.
- Roden, G.I., 1994: Effects of the Fieberling seamount group upon flow and thermohaline structure in the spring of 1991, *J. Geophys. Res.*, 99, 9941–9961.
- Sanford, T.B., R.G. Drever, J.H. Dunlap and E.A. D'Asaro, 1982: Design, operation and performance of an expendable temperature and velocity profiler (XTVP), Tech. Rpt. 8110, Appl. Phys. Lab, Univ. of Wash., Seattle, WA 83 pp.
- Sanford, T.B., E.A. D'Asaro, E. Kunze, J.H. Dunlap, R.G. Drever, M.A. Kennelly, M.D. Prater and M.S. Horgan, 1993: An XCP user's guide and reference manual, Tech. Rpt. APL-UW TR 9309, Appl. Phys. Lab, Univ. of Washington, Seattle, WA, 59 pp.
- Schmitt, R.W., J.M. Toole, R.L. Koehler, E.C. Mellinger, and K.W. Doherty, 1988: The development of a fine- and microstructure profiler, *J. Ocean Atmos. Technol.*, 5, 484–500.
- Schwidorski, E.W., 1981a: Global ocean tides, Part IV: The diurnal luni-solar declination tide (K_1). Atlas of tidal charts and maps, TR81-142, Naval Surface Weapons Center, Dahlgren, VA.
- Schwidorski, E.W., 1981b: Global ocean tides, Part V: The diurnal principal lunar tide (O_1). Atlas of tidal charts and maps, TR81-142, Naval Surface Weapons Center, Dahlgren, VA.
- Swaters, G.E., and L.A. Mysak, 1985: Topographically induced baroclinic eddies near a coastline with application to the Northeast Pacific, *J. Phys. Oceanogr.*, 15, 1470–1485.
- Toole, J.M., K.L. Polzin and R.W. Schmitt, 1994: Estimates of diapycnal mixing in the abyssal ocean, *Science*, 264, 1120–1123.
- Toole, J.M., R.W. Schmitt, K.L. Polzin, and E. Kunze, 1995: Fine- and microstructure observations of boundary mixing on the flanks of Fieberling Guyot, in preparation.

- Verron, J., and C. LeProvost, 1985: A numerical study of quasi-geostrophic flow over isolated topography, *J. Fluid Mech.*, 154, 231–252.
- Weller, R.A., 1982: The relation of near-inertial motions observed in the mixed-layer during the JASIN (1978) experiment to the local wind stress and to the quasigeostrophic flow field, *J. Phys. Oceanogr.*, 12, 1122–1136.
- Wichman, C.A., C.C. Eriksen, N.M. Bogue, K.H. Brink, D.E. Frye, R.D. Pillsbury, G.M. Pittock, and S.A. Tarbell, 1993: Fieberling Guyot moored array data, Tech. Rpt. A93-1,

- School of Oceanography, University of Washington, Seattle, WA, 373 pp.
- Wunsch, C., 1969: Progressive internal waves on slopes, *J. Fluid Mech.*, 35, 131–144.
- Zhang, X., and D.L. Boyer, 1993: Laboratory study of rotating, stratified, oscillatory flow over a seamount, *J. Phys. Oceanogr.*, 23, 1122–1141.
- Zyryanov, V.N., 1981: A contribution to the theory of Taylor columns in a stratified ocean, *Izvestiya, Atmos. Ocean Phys.*, 17, 793–800.

Appendix A: Vortex-Trapped Near-Inertial Waves

Following Kunze *et al.* 1995), consider the equations of motion for a hydrostatic ($\omega_i \ll N$) internal wave of the form $\psi = \psi_0(r) \cdot \exp[i(n\theta + k_z z - \omega_e t)]$, where n is the azimuthal mode number, k_z the vertical wavenumber, and ω_e the invariant Eulerian frequency, inside an axisymmetric vortex $V_\theta(r)$

$$\begin{aligned} -i \left[\omega_E - \frac{nV_\theta}{r} \right] u_r - \left[f + \frac{2V_\theta}{r} \right] v_\theta &= -\frac{\partial p}{\partial r} \\ -i \left[\omega_E - \frac{nV_\theta}{r} \right] v_\theta + \left[f + \frac{V_\theta}{r} + \frac{\partial V_\theta}{\partial r} \right] u_r &= -\frac{in p}{r} \\ 0 &= -ik_z p + b \Rightarrow p = \frac{-N^2 w}{\omega_i k_z} \quad (A1) \\ -i \left[\omega_E - \frac{nV_\theta}{r} \right] b + N^2 w &= 0 \Rightarrow b = \frac{-iN^2 w}{\omega_i} \end{aligned}$$

$$\frac{1}{r} \frac{\partial(nu_r)}{\partial r} + \frac{inv_\theta}{r} + ik_z w = 0,$$

where (u_r, v_θ, w) are the radial, azimuthal and vertical wave velocities, V_θ the mean azimuthal velocity, $b = -N^2 \xi$ the wave-induced buoyancy anomaly, p the wave-induced pressure, and the intrinsic frequency $\omega_i = \omega_E - nV_\theta/r$. Assuming that the buoyancy frequency depends only weakly on radius, the radial derivatives of ω_i and p are

$$\frac{\partial \omega_i}{\partial r} = \frac{n}{r} \left[\frac{V_\theta}{r} - \frac{\partial V_\theta}{\partial r} \right] \quad (A2)$$

$$\frac{\partial p}{\partial r} = -\frac{N^2}{\omega_i k_z} \frac{\partial w}{\partial r} + \frac{nN^2}{\omega_i^2 k_z r} \left(\frac{V_\theta}{r} - \frac{\partial V_\theta}{\partial r} \right) w. \quad (A3)$$

Thus, the two horizontal momentum equations in (A1) can be expressed

$$-i\omega_i u_r - \left[f + \frac{2V_\theta}{r} \right] v_\theta = \frac{N^2}{\omega_i k_z} \frac{\partial w}{\partial r} - \frac{nN^2}{\omega_i^2 k_z r} \left(\frac{V_\theta}{r} - \frac{\partial V_\theta}{\partial r} \right) w$$

(A4)

$$-i\omega_i v_\theta + \left[f + \frac{V_\theta}{r} + \frac{\partial V_\theta}{\partial r} \right] u_r = i \frac{nN^2}{\omega_i k_z r} w.$$

The azimuthal momentum equation implies

$$v_\theta = -i \left[\frac{f + V_\theta/r + \partial V_\theta/\partial r}{\omega_i} \right] u_r - \frac{nN^2}{\omega_i^2 k_z r} w \quad (A5)$$

which, when substituted into the radial momentum equation and continuity, yields

$$\begin{aligned} -i\omega_i k_z r \left[\omega_i^2 - (f + 2V_\theta/r)(f + V_\theta/r + \partial V_\theta/\partial r) \right] u_r \\ = N^2 \omega_i r \frac{\partial w}{\partial r} - nN^2 (f + 3V_\theta/r - \partial V_\theta/\partial r) w \end{aligned} \quad (A6)$$

$$\begin{aligned} w &= -i \left[\frac{\omega_i^2 k_z r}{n^2 N^2 - \omega_i^2 k_z^2 r^2} \right] \frac{\partial(nu_r)}{\partial r} \\ &\quad - i \left[\frac{n\omega_i k_z r (f + V_\theta/r + \partial V_\theta/\partial r)}{n^2 N^2 - \omega_i^2 k_z^2 r^2} \right] u_r. \end{aligned}$$

For an azimuthal mode $n = -1$, $n^2 N^2 \ll \omega_i^2 k_z^2 r^2$ provided $r \gg N\lambda_z/(2\pi\omega_i) \simeq 3$ km for $N = 5 \times 10^{-3} \text{ s}^{-2}$, $\lambda_z = 210$ m and $\omega = K_1 + \zeta/2 = 5.7 \times 10^{-5} \text{ s}^{-1}$. Except in the inner core, the vertical velocity w can be simplified to

$$w = \frac{i}{k_z} \frac{\partial u_r}{\partial r} + i \left[\frac{\omega_i + n(f + V_\theta/r + \partial V_\theta/\partial r)}{\omega_i k_z r} \right] u_r \quad (A7)$$

with radial derivative

$$\begin{aligned} \frac{\partial w}{\partial r} &= \frac{i}{k_z} \frac{\partial^2 u_r}{\partial r^2} + i \left[\frac{\omega_i + n(f + V_\theta/r + \partial V_\theta/\partial r)}{\omega_i k_z r} \right] \frac{\partial u_r}{\partial r} \\ &\quad + i \left[\frac{n}{\omega_i k_z r} \frac{\partial^2 V_\theta}{\partial r^2} \right] u_r \end{aligned} \quad (A8)$$

$$- \left(\frac{[\omega_i + n(f + \frac{V_\theta}{r} + \frac{\partial V_\theta}{\partial r})][\omega_i + n(\frac{V_\theta}{r} - \frac{\partial V_\theta}{\partial r})]}{\omega_i^2 k_z r^2} \right) u_r.$$

Substituting w (A7) and $\partial w/\partial r$ (A8) into (A6),

$$\begin{aligned} \frac{\partial^2 u_r}{\partial r^2} + \left[\frac{\omega_i - 2n(V_\theta/r - \partial V_\theta/\partial r)}{\omega_i r} \right] \frac{\partial u_r}{\partial r} + \\ \left\{ \frac{n}{\omega_i r} \frac{\partial^2 V_\theta}{\partial r^2} + \frac{[\omega_i^2 - (f + 2V_\theta/r)(f + V_\theta/r + \partial V_\theta/\partial r)]k_z^2}{N^2} - \right. \\ \left. \frac{[\omega_i + n(f + V_\theta/r + \partial V_\theta/\partial r)][\omega_i + n(f + 4V_\theta/r - 2\partial V_\theta/\partial r)]}{\omega_i^2 r^2} \right\} \end{aligned} \quad (A9)$$

$$\times u_r = 0.$$

A.1 Application

Consider a vortex containing a core in solid-body rotation ζ inside radius $r = r_o$ and azimuthal velocities falling off as r^{-1} outside the velocity maximum ($\zeta = 0$). Also recall that the observed wave has azimuthal mode $n = -1$ corresponding to clockwise propagation around the vortex.

A.2 Inside the Core

For $r < r_o$, $V_\theta = \zeta r/2$, $V_\theta/r = \partial V_\theta/\partial r = \zeta/2$, and $\partial^2 V_\theta/\partial r^2 = 0$ so that (A9) can be simplified to

$$\begin{aligned} \frac{\partial^2 u_r}{\partial r^2} + \frac{1}{r} \frac{\partial u_r}{\partial r} + \left[\frac{(\omega_i^2 - f_{\text{eff}}^2)k_z^2}{N^2} - \frac{(\omega_i - f_{\text{eff}})^2}{\omega_i^2 r^2} \right] u_r = 0 \end{aligned}$$

which, in the context of our previous assumption that $r \gg N/(\omega_i k_z)$ or recognizing that $\omega_i - f_{\text{eff}} \ll \omega_i$ for the near-inertial waves of interest here, simplifies further to

$$\frac{\partial^2 u_r}{\partial r^2} + \frac{1}{r} \frac{\partial u_r}{\partial r} + \frac{(\omega_i^2 - f_{\text{eff}}^2)k_z^2}{N^2} u_r = 0 \quad (A10)$$

where $f_{\text{eff}} = f + \zeta$ as found by Kunze *et al.* (1995). This has $J_0(k_r r)$ Bessel function solutions for $\omega_i > f_{\text{eff}}$ where the radial cylindrical “wavenumber”

$$k_r = \frac{k_z \sqrt{\omega_i^2 - f_{\text{eff}}^2}}{N}.$$

A.3 Outside the Core

For $r > r_o$, $V_\theta = \zeta r_o^2/(2r)$, $V_\theta/r = \zeta r_o^2/(2r^2)$, $\partial V_\theta/\partial r = -\zeta r_o^2/(2r^2)$, $\partial V_\theta/\partial r^2 = \zeta r_o^2/r^3$ where ζ is the core vorticity, and (A9) can be simplified to

$$0 = \frac{\partial^2 u_r}{\partial r^2} + \left[\frac{1}{r} + \frac{2\zeta r_o^2}{\omega_i r^3} \right] \frac{\partial u_r}{\partial r} + \left[\frac{(\omega_i^2 - f(f + \zeta r_o^2/r^2))k_z^2}{N^2} - \frac{\omega_i^2 - 2\omega_i(f + \zeta r_o^2/r^2) + f(f + 3\zeta r_o^2/r^2)}{\omega_i^2 r^2} \right] u_r.$$

For $r \gg N/(\omega_i k_z)$, this can be approximated as

$$\frac{\partial^2 u_r}{\partial r^2} + \left[\frac{1}{r} + \frac{2\zeta r_o^2}{\omega_i r^3} \right] \frac{\partial u_r}{\partial r} + \left[\frac{(\omega_i^2 - f(f + \zeta r_o^2/r^2))k_z^2}{N^2} \right] u_r = 0 \quad (A11)$$

which becomes a modified Bessel equation

$$\frac{\partial^2 u_r}{\partial r^2} + \frac{1}{r} \frac{\partial u_r}{\partial r} + \left[\frac{(\omega_i^2 - f^2)k_z^2}{N^2} \right] u_r = 0$$

with trapped solutions $K_0(k_o r)$ where $k_o = k_z \sqrt{f^2 - \omega_i^2}/N$ as $r \rightarrow \infty$ for $\omega_i < f$.

A vortex-trapped near-inertial wave will have Bessel function solutions inside the core ($r < r_o$, $\omega_i > f_{\text{eff}}$) (A10) and distorted modified Bessel function solutions outside the core ($r > r_o$, $\omega_i < f$) (A11). Finding trapped radial modes involves matching the Eulerian frequency $\omega_E = K_1$, the vertical wavelength λ_z , the azimuthal mode number n , the radial velocity u_r , and the radial divergence $\partial(nu_r)/\partial r$ at $r = r_o$. Kunze *et al.* (1995) neglected terms involving $\zeta r_o^2/r^2$ in (A11) so that analytic solutions $J_0(k_r r)$ and $K_0(k_o r)$ could be matched. This was also done for the envelope of solutions displayed in Fig. 16 which correspond to the observed range of buoyancy frequency $N = (4-5) \times 10^{-3} \text{ s}^{-1}$, core radius $r_o = 5-7 \text{ km}$, core vorticity $-0.52f$ to $-0.45f$, vertical wavelength $\lambda_z = 170-220 \text{ m}$ and Eulerian frequency $\omega_E = K_1$. Neglecting the straining terms $\zeta r_o^2/r^2$ in (A11) will have a slight effect on the inner radial wavelengths $2\pi/k_r$ and the outer radial decay lengths $2\pi/k_o$ but this has not yet been quantified.

Appendix B: Viscous Near-Inertial Waves

Consider the equations of motion for hydrostatic rectilinear internal waves of the form $\psi = \psi_0(r) \exp[i(k_x x + k_z z - \omega t)]$, where $\mathbf{k} = (k_x, 0, k_z)$ is the wavevector chosen so the horizontal direction of propagation lies along the x -axis ($k_y = 0$) and ω the intrinsic frequency damped by eddy viscosity ν_e and eddy diffusivity κ_e ,

$$-i\omega_i u - fv = -ik_x p + \nu_e k_z^2 u$$

$$-i\omega_i v + fu = \nu_e k_z^2 v$$

$$0 = -ik_z p + b$$

$$\Rightarrow p = \frac{-ib}{k_z} \quad (B1)$$

$$-i\omega_i b + N^2 w = \kappa_e k_z^2 b \quad \Rightarrow \quad b = \frac{-iN^2 w}{(\omega_i - i\kappa_e k_z^2)}$$

$$k_x u + k_z w = 0 \quad \Rightarrow \quad w = \frac{-k_x u}{k_z}$$

so that

$$[\omega_i - i\nu_e k_z^2] \cdot u - fv = \frac{N^2 k_x^2 \cdot u}{(\omega_i - i\kappa_e k_z^2) k_z^2} \quad (B2)$$

$$-[i\omega_i + \nu_e k_z^2] \cdot v + fu = 0 \quad \Rightarrow \quad v = \frac{-ifu}{(\omega_i - i\nu_e k_z^2)}$$

and the buoyancy is

$$b = \frac{iN^2 k_x u}{(\omega_i - i\kappa_e k_z^2) k_z} \quad (B3)$$

Substituting the boxed expression for v in (B2) into the first expression in (B2) and assuming weakly-damped ($\nu_e k_z^2, \kappa_e k_z^2 \ll f$) near-inertial ($N^2 k_x^2 \ll f^2 k_z^2$) waves, the dispersion relation can be approximated by

$$\omega = f + \frac{N^2 k_x^2}{2fk_z^2} + i\nu_e k_z^2 \quad (B4)$$

The effect of viscosity appears as a weak evanescence in time (or in the direction of energy propagation \mathbf{C}_g). Within the context of this approximation, the eddy diffusivity has no impact on the dispersion relation because near-inertial waves have relatively weak buoyancy signals. More general viscous internal wave behavior can be found in LeBlond (1966). For $\nu_e = 10 \times 10^{-4} \text{ m}^2 \text{ s}^{-1}$ and $\lambda_z = 100\text{--}300 \text{ m}$, $\nu_e k_z^2 = (0.4\text{--}4.0) \times 10^{-6} \text{ s}^{-1}$ so is much smaller than the Coriolis frequency $f = 7.8 \times 10^{-5} \text{ s}^{-1}$. Substituting the dispersion relation (B4) into (B3) and (B2), we obtain the following consistency relations between the buoyancy b , north velocity v , and east velocity u :

$$b = \frac{N^2 k_x}{fk_z} \left[i - i \frac{N^2 k_x^2}{2f^2 k_z^2} + \frac{(\nu_e - \kappa_e) k_z^2}{f} \right] \cdot u \quad (B5)$$

$$v = -i \left[1 - \frac{N^2 k_x^2}{2f^2 k_z^2} \right] \cdot u.$$

The phase relations between uv , ub and vb are then

$$\phi_{uv} = \frac{\pi}{2}$$

$$\phi_{ub} = \text{Arctan} \left[\frac{2f^2 k_z^2 - N^2 k_x^2}{2fk_z^2(\nu_e - \kappa_e)k_z^2} \right] \quad (B6)$$

$$\approx \text{Arctan} \left[\frac{f}{(\nu_e - \kappa_e)k_z^2} \right]$$

$$\phi_{vb} = \text{Arctan} \left[\frac{-(\nu_e - \kappa_e)k_z^2}{f} \right],$$

so that the two horizontal velocity components remain 90° out of phase but the velocity and buoyancy perturbations have slightly modified phase relations if the eddy viscosity and diffusivity differ from zero and each other (eddy Prandtl number $\nu_e/\kappa_e \neq 1.0$). For an eddy viscosity $\nu_e = 10 \times 10^{-4} \text{ m}^2 \text{ s}^{-1}$ and $\lambda_z = 100 \text{ m}$, the phase relations differ by at most 3° from their inviscid values. These are shown in Fig. 17 for Prandtl numbers ranging from zero to infinity.

Appendix C: Viscous Stratified Topographic Waves

Following Rhines (1970) and Appendices A and B, the equations of motion for stratified bottom-trapped topographic waves with eddy viscous ν_e and diffusive κ_e forcing on gentle slopes ($\alpha \ll 1$) are

$$\begin{aligned} -i(\omega - i\nu_e k_\perp^2)u_\parallel - fv &= -ik_\parallel p + b\alpha \\ -i(\omega - i\nu_e k_\perp^2)v + fu_\perp &= -ik_y p \\ f\alpha v &= -ik_\perp p + b \end{aligned} \quad (C1)$$

$$-i(\omega - i\kappa_e k_\perp^2)b = -N^2 \alpha u_\parallel \quad \Rightarrow \quad b = \frac{-iN^2 \alpha u_\parallel}{(\omega - i\kappa_e k_\perp^2)}$$

$$k_\parallel u_\parallel + k_y v = 0 \quad \Rightarrow \quad v = \frac{-k_\parallel u_\parallel}{k_y},$$

where (u_\parallel, v) are the across- and along-isobath velocities parallel to the bottom, the flow normal to the bottom w_\perp is assumed to vanish identically, and $(k_\perp, k_y, k_\parallel)$ are the across-isobath, along-isobath and normal wavenumbers in a coordinate system lying in the plane of the bathymetry. It has been assumed that $k_\perp \gg k_\parallel, k_y$ in the viscous terms consistent with the observations. Substituting the boxed expressions for buoyancy b and along-isobath velocity v into the first three expressions of (C1),

$$\begin{aligned} \left[\frac{-i(\omega - i\nu_e k_\perp^2)}{k_\parallel} + \frac{f}{k_y} + \frac{iN^2 \alpha^2}{(\omega - i\kappa_e k_\perp^2)k_\parallel} \right] u_\parallel &= -ip \\ \left[\frac{i(\omega - i\nu_e k_\perp^2)k_\parallel}{k_y^2} + \frac{f}{k_y} \right] u_\parallel &= -ip \end{aligned} \quad (C2)$$

$$\left[\frac{-f\alpha k_\parallel}{k_y k_\perp} + \frac{iN^2 \alpha}{(\omega - i\kappa_e k_\perp^2)k_\perp} \right] u_\parallel = -ip$$

or, equating the lefthand sides,

$$\begin{aligned}
(\omega - i\nu_e k_\perp^2)(\omega - i\kappa_e k_\perp^2) &= \frac{N^2 \alpha^2 k_y^2}{k_H^2} \\
(\omega - i\nu_e k_\perp^2)(\omega - i\kappa_e k_\perp^2) k_1 k_\perp & \quad (C3) \\
- if k_y k_\perp (\omega - i\kappa_e k_\perp^2) - N^2 \alpha k_y^2 &= 0,
\end{aligned}$$

which can be solved for ω and k_\perp in terms of $N, f, \alpha, \nu_e, \kappa_e, k_y$ and k_\parallel . Assuming that the frequency ω is changed only slightly so that it can be expressed in terms of the inviscid solution $\omega = N\alpha k_y/k_H + \delta\omega$, where $\delta\omega \ll N\alpha k_y/k_H$, the first equation in (C3) implies

$$\omega \simeq \frac{N\alpha k_y}{k_H} + \frac{i(\nu_e + \kappa_e)k_\perp^2}{2} \quad (C4)$$

where $N\alpha k_y/k_H \simeq f \gg \nu_e k_\perp^2, \kappa_e k_\perp^2$ from before. Substituting (C4) into the second equation in (C3) gives

$$\begin{aligned}
\frac{N^2 \alpha^2 k_y k_\parallel k_\perp}{k_H^2} - if k_\perp \left(\frac{N\alpha k_y}{k_H} + \frac{i(\nu_e - \kappa_e)k_\perp^2}{2} \right) \\
- N^2 \alpha k_y = 0 \quad (C5)
\end{aligned}$$

and, assuming a solution for k_\perp perturbed about the inviscid solution

$$k_\perp = \frac{Nk_H^2}{N\alpha k_\parallel - if k_H} = Nk_H^2 \frac{N\alpha k_\parallel + if k_H}{N^2 \alpha^2 k_\parallel^2 + f^2 k_H^2}, \quad (C6)$$

leads to a viscous perturbation

$$\delta k_\perp = \frac{N^2 f (\nu_e - \kappa_e) k_H^8}{2\alpha k_y (N\alpha k_\parallel - if k_H)^4}. \quad (C7)$$

This could blow up if $k_y = 0$, invalidating the small perturbation approximation. Based on the observational results of a diurnal Eulerian frequency $\omega_E = K_1$ and an imaginary vertical wavenumber at most comparable to the real vertical wavenumber, $k_z \simeq \text{Re}\{k_\perp\}$, we can quantify the relationship between buoyancy b and u_\parallel in (C1)

$$b \simeq \frac{-iN^2 \alpha u_\parallel}{f + \frac{i(\nu_e - \kappa_e)k_\perp^2}{2}} \simeq \frac{-N^2 \alpha}{f} \left[\frac{(\nu_e - \kappa_e)k_z^2}{2f} + i \right] u_\parallel \quad (C8)$$

so the phase relation between u_\parallel and b becomes

$$\phi_{ub} = \text{Arctan} \left(\frac{2f}{(\nu_e - \kappa_e)k_z^2} \right) \quad (C9)$$

perturbed from the inviscid solution by half the amount that viscous near-inertial waves are perturbed from their inviscid solution. We apply viscous phase relation offsets (B6) and (C9) to seamount- and vortex-trapped waves under the assumption that the geometry is not a major consideration.